



## Simulated Evolution and Severe Wind Production by the 25–26 June 2015 Nocturnal MCS from PECAN<sup>✉</sup>

MATTHEW D. PARKER AND BRETT S. BORCHARDT<sup>a</sup>

*North Carolina State University, Raleigh, North Carolina*

RACHEL L. MILLER AND CONRAD L. ZIEGLER

*NOAA/National Severe Storms Laboratory, Norman, Oklahoma*

(Manuscript received 19 March 2019, in final form 26 August 2019)

### ABSTRACT

The 25–26 June 2015 nocturnal mesoscale convective system (MCS) from the Plains Elevated Convection at Night (PECAN) field project produced severe winds within an environment that might customarily be associated with elevated convection. This work incorporates both a full-physics real-world simulation and an idealized single-sounding simulation to explore the MCS's evolution. Initially, the simulated convective systems were elevated, being maintained by wavelike disturbances and lacking surface cold pools. As the systems matured, surface outflows began to appear, particularly where heavy precipitation was occurring, with air in the surface cold pools originating from up to 4–5 km AGL. Via this progression, the MCSs exhibited a degree of self-organization (i.e., structures that are dependent upon an MCS's particular history). The cold pools eventually became 1.5–3.5 km deep, by which point passive tracers revealed that the convection was at least partly surface based. Soon after becoming surface based, both simulations produced severe surface winds, the strongest of which were associated with embedded low-level mesovortices and their attendant outflow surges and bowing segments. The origin of the simulated mesovortices was likely the downward tilting of system-generated horizontal vorticity (from baroclinity, but also possibly friction) within the simulated MCSs' outflow, as has been argued in a number of previous studies. Taken altogether, it appears that severe nocturnal MCSs may often resemble their cold pool-driven, surface-based afternoon counterparts.

### 1. Introduction

It has long been known that the central United States has a nocturnal maximum in summertime convective precipitation (e.g., Wallace 1975; Carbone et al. 2002), and that this maximum primarily reflects recurring organized mesoscale convective systems (MCSs; Maddox 1980; Fritsch et al. 1986). In addition to their integrated seasonal rainfall, Schumacher and Johnson (2006) showed

that nocturnal MCSs produce a large fraction of local warm season extreme precipitation events (e.g., flash floods). A substantial number of warm season derechos (severe, long-lived convective wind storms) have also been associated with nocturnal MCSs (e.g., Johns and Hirt 1987). Given their societal importance, it is unsatisfying that predictions of nocturnal convective systems have typically lagged in comparison to other kinds of precipitation systems (Olson et al. 1995; Davis et al. 2003; Fritsch and Carbone 2004; Weisman et al. 2008; Peters et al. 2017).

Nocturnal environments often exhibit a shallow statically stable boundary layer (SBL) and substantial evolution of the near-ground wind profile, including a developing low-level jet (e.g., Stull 1988). Climatologies also reveal that nocturnal MCSs often occur on the cool side of warm or stationary fronts (e.g., Augustine and Caracena 1994; Laing and Fritsch 2000), locations

<sup>✉</sup> Supplemental information related to this paper is available at the Journals Online website: <https://doi.org/10.1175/MWR-D-19-0072.s1>.

<sup>a</sup> Current affiliation: NOAA/National Weather Service, Grand Rapids, Michigan.

Corresponding author: Matthew D. Parker, [mdparker@ncsu.edu](mailto:mdparker@ncsu.edu)

that may have even deeper layers of strong stability. Given a SBL, it has often been presumed that most nocturnal MCSs comprise elevated convection (e.g., Colman 1990; Parker 2008); this would imply that such systems are only ingesting air parcels that originate from above the SBL. Along these lines, there are examples of nocturnal MCSs passing by surface stations with negligible fluctuations in surface temperature (e.g., Maddox 1980; Trier and Parsons 1993), which may mean that such systems lack surface cold pools and are almost totally decoupled from the SBL. This would represent a departure from the classical density current-driven model of organized (diurnal) multicellular convection (the “long-lived squall lines” described by Rotunno et al. 1988, the “type-2” events reviewed by Fritsch and Forbes 2001, etc.). Therefore, it has often been argued that nocturnal MCSs are instead sustained by internal bores or gravity waves (Dudhia et al. 1987; Crook and Moncrieff 1988; Schmidt and Cotton 1989; Buzzi et al. 1991; Haertel et al. 2001; Fovell et al. 2006; Parker 2008; Schumacher 2009; Browning et al. 2010; French and Parker 2010; Marsham et al. 2010; Blake et al. 2017; Parsons et al. 2019).

Notably, however, some studies have suggested that nocturnal MCSs may still be surface based (i.e., ingesting air from the SBL) notwithstanding the strong nocturnal static stability. Parker (2008), French and Parker (2010), and Billings and Parker (2012) found that, if early evening convection was able to establish a surface cold pool, an MCS could continue to ingest near-surface air even after considerable nocturnal stabilization occurred. Marsham et al. (2011) provided an example in which initially elevated convection was able to build up a surface cold pool and subsequently transition to surface-based convection. These findings are quite pertinent given the PECAN observations presented by Hitchcock et al. (2019), which showed that nearly every observed nocturnal MCS had a surface cold pool (some as strong as  $-9\text{ K}$  and as deep as 4 km). As reviewed by Corfidi et al. (2008), convective storms exist on a continuum and may ingest air from multiple source layers, making even the binary distinction between surface-based and elevated convection somewhat ambiguous. Ultimately, the kinematic structures and governing dynamics of nocturnal MCSs have remained somewhat elusive, perhaps because of the challenges of effectively observing storms that may or may not be decoupled from the surface.

These scientific questions motivated the Plains Elevated Convection at Night (PECAN) field project in 2015. As reviewed by Geerts et al. (2017), PECAN targeted a range of nocturnal mesoscale phenomena, including convective initiation, bores, the low-level jet,

nocturnal MCSs, and nocturnal convective predictability. Among the investigators focusing on nocturnal MCSs, the primary scientific objectives were to (i) document and analyze the evolution of nocturnal MCSs and system structures, and (ii) to establish the environmental ingredients and related physical mechanisms that control nocturnal MCS evolution.

The 25–26 June 2015 intensive observing period (IOP) provided the opportunity to study a quasi-linear convective system (QLCS) that was particularly relevant to the aforementioned objectives. Convection was initiated in eastern Nebraska and Kansas and then moved through the array of PECAN measurement platforms (generally surrounding the PECAN soundings site plotted in Fig. 1). PECAN soundings depicted a layer of enhanced stability extending from just above the surface through 850 hPa (Fig. 2), which was associated both with a prior frontal passage (front annotated in Fig. 1) and modest nocturnal cooling. Due to this stable layer, the most unstable (MU) parcels were located more than 1 km above the surface, having  $\text{CAPE} > 2000\text{ J kg}^{-1}$  and negligible CIN, whereas surface-based (SB) air parcels had considerably less CAPE along with CIN magnitudes in excess of  $100\text{ J kg}^{-1}$  (Fig. 3, blue and green profiles). Such an environment would commonly be assumed to support elevated, but not surface-based convection.

Despite the layer of enhanced lower tropospheric stability present during the 25–26 June 2015 IOP, the resulting MCS went on to produce nearly 50 severe wind reports [winds exceeding 50 kt ( $1\text{ kt} \approx 0.5144\text{ m s}^{-1}$ ), or  $\approx 26\text{ m s}^{-1}$ ] in northeastern Kansas and western Missouri, including several estimated gusts exceeding  $30\text{ m s}^{-1}$  (Fig. 1). Horgan et al. (2007) discussed the substantial challenges of severe wind forecasting in this scenario. One testable hypothesis is that the 25–26 June MCS remained elevated and lacked a substantial surface cold pool. In such a case, severe winds might result either from the lifting and subsequent descent of air parcels within the near-surface stable layer (e.g., the “up–down” trajectories of Schmidt and Cotton 1989; Knupp 1996; Bernardet and Cotton 1998; MacIntosh and Parker 2017), or via the pressure gradient accelerations associated with static features above or gravity waves within the stable layer (e.g., Bosart and Seimon 1988; Schmidt and Cotton 1989). An alternative possibility is that the 25–26 June MCS produced a cold pool and potentially became surface based (much as in the study of Marsham et al. 2011), at which point it would presumably produce severe winds via more classical mechanisms (e.g., Wakimoto 2001; Trapp and Weisman 2003).

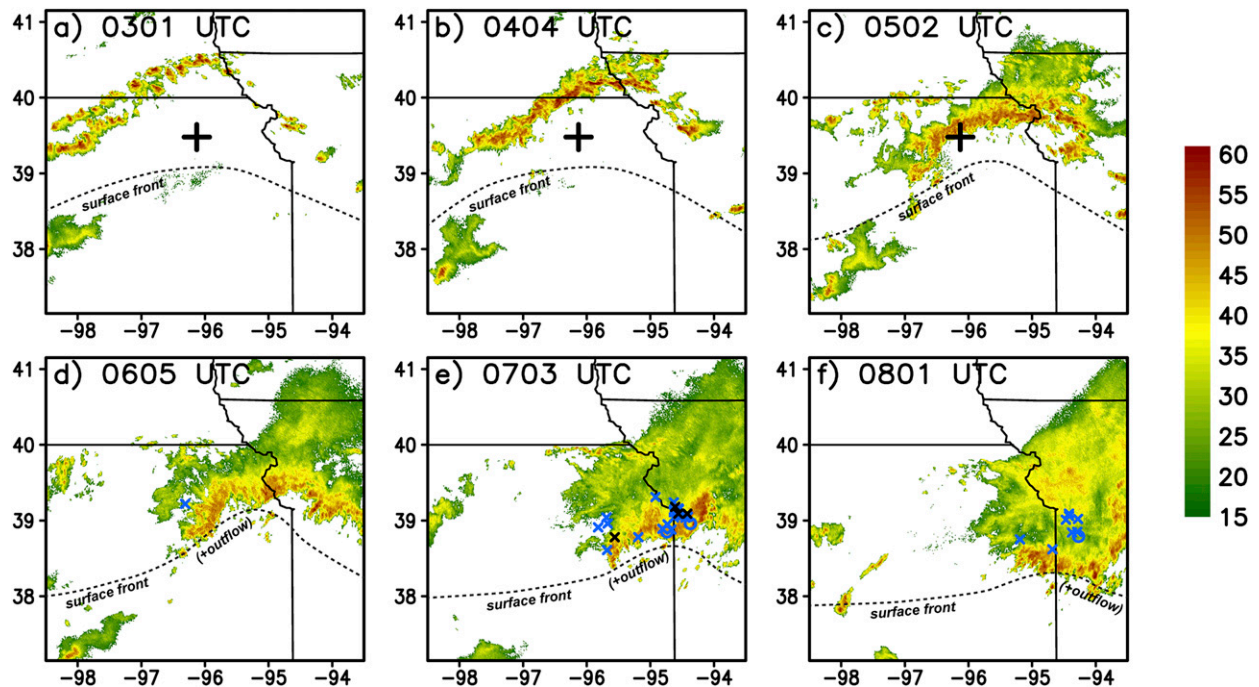


FIG. 1. Observed base scan logarithmic radar reflectivity factor (shaded, dBZ) from Topeka, KS (KTWX), at approximately hourly intervals on 26 Jun 2015, with severe wind reports from the hour preceding each image. Measured severe winds are plotted with a circle, while severe wind reports with estimated or missing winds are plotted with an  $\times$ ; significant severe wind reports (winds  $\geq 65$  kt, or  $\approx 34$   $\text{m s}^{-1}$ ) are colored black (all other reports are colored blue). The location of the 0300 UTC and 0430 UTC observed soundings from PECAN (Figs. 2 and 3) is shown with a black cross in the upper panels. The location of the primary surface front at each hour is annotated with a dashed curve (at later times it is largely merged with an outflow boundary produced by the MCS).

The early stages of the event were rather well-observed by PECAN's instrumentation, and the anatomy of the observed MCS (including multi-Doppler radar wind syntheses) was presented in detail by Miller et al. (2019). The present experiments are motivated by these 25–26 June PECAN observations, and are designed to isolate key processes relevant to the observed MCS's evolution. We seek to understand the development of surface outflows, the possible transition from elevated toward surface-based convection, and the subsequent production of mesovortices, bowing structures, and severe surface winds, to the extent that they occur within the simulations. The long-range goal is to shed light on the dynamics and predictability of nocturnal MCSs (and associated severe weather), topics that would be comparatively harder to address using the observations alone. To assess the comparative roles of the large-scale setting versus convective self-organization, we incorporate both full-physics real-world and idealized single-sounding simulations.

Section 2 of this article documents the configurations for the two sets of simulations analyzed in this study. In section 3, we provide a basic overview of the observed 25–26 June case and how it compares to the real-world

and idealized simulations. Section 4 focuses on the evolution of both simulated systems from initially elevated convection toward subsequently surface-based, cold pool-driven MCSs, while section 5 details the mechanisms for production of severe surface winds associated with mesovortices in both simulations. We conclude in section 6 by combining the simulation results into a conceptual model for the 25–26 June MCS's evolution.

## 2. Methods

Miller et al. (2019) documented the observed structures during the first 3–4 h of the 25–26 June 2015 MCS using surface observations, soundings, and multi-Doppler radar wind syntheses. With those observations as motivation, we utilized both the Advanced Research core of the Weather Research and Forecasting (WRF) Model (the WRF-ARW; Klemp et al. 2007; Skamarock and Klemp 2008; Skamarock et al. 2008) and the Bryan Cloud Model (CM1; Bryan and Fritsch 2002; Bryan and Morrison 2012) for the present process study. The details of each model's settings are described in Table 1. Each model's simulation was attempted with both the

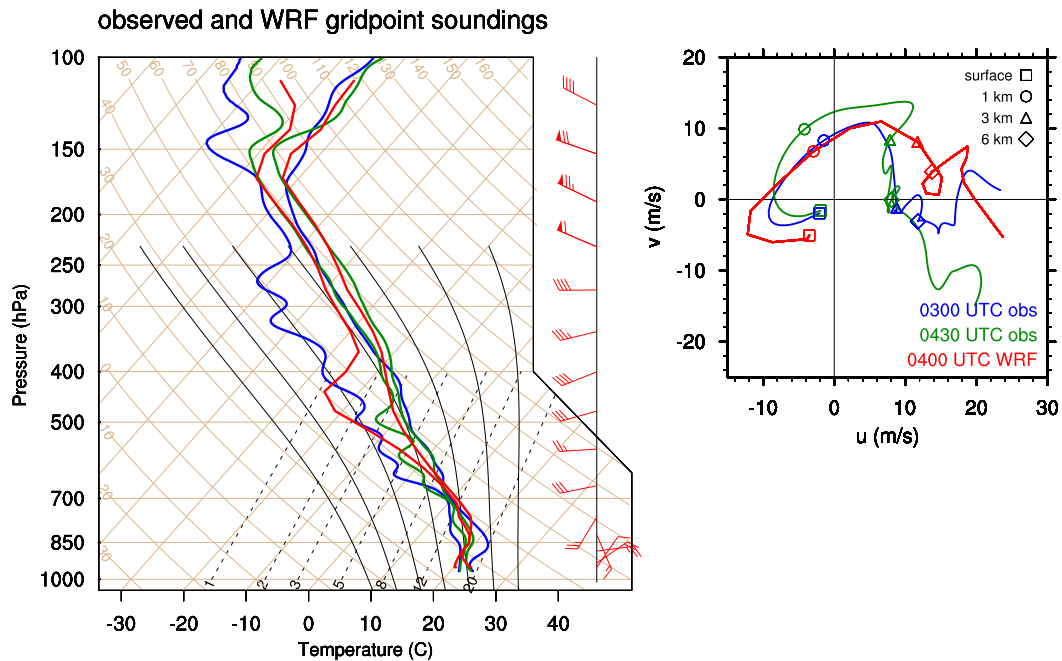


FIG. 2. (left) Skew  $T$ -log $p$  diagram of temperature and humidity and (right) hodograph diagram of wind vectors for the three soundings described in this study. All data from the 0300 UTC 26 Jun 2015 PECAN observation are plotted in blue. All data from the 0430 UTC 26 Jun 2015 PECAN observation are plotted in green. All data from the 0400 UTC WRF Model gridpoint sounding are plotted in red. Wind barbs (barb =  $5 \text{ m s}^{-1}$ , flag =  $25 \text{ m s}^{-1}$ ) are plotted for the 0400 UTC WRF sounding only. The location of the PECAN soundings is indicated in Figs. 1a–c and 4d. The location of the WRF gridpoint sounding is indicated in Fig. 6a. Vertical profiles of CAPE, CIN, and  $\Delta z_{\text{LFC}}$  for these soundings are shown in Fig. 3. The observed PECAN soundings were passed through a simple vertical smoother (the same procedure used by Parker 2014) to remove noise before plotting.

Thompson et al. (2008) and Morrison et al. (2009) microphysical parameterizations (not shown), with the more realistic simulation from each model selected for formal analysis. Some additional details and caveats are provided in the remainder of this section.

#### a. Real-world WRF simulation

The “real-world” simulation used version 3.6 of the WRF-ARW model. The simulations ultimately included 4 nested grids (details in Table 1), whose boundaries are shown in Fig. 4a. The outermost domain was initialized at 0000 UTC 25 June 2015, which was more than 24 h before the development of the convective storms studied by PECAN. The 3-km domain was then launched at 1800 UTC, followed by the 1-km and 333-m domains at 0000 UTC 26 June 2015 (still several hours before the primary MCS developed). The physical parameterizations are summarized in Table 1, with convective motions treated explicitly on all grids except for the outermost 15-km domain.

To assess the origins of air parcels in both the updrafts and outflows of simulated convective storms, passively advected tracers were introduced in 500-m-deep

layers extending from the surface through 6 km AGL. However, in time, the boundary layer parameterization caused the tracers to become heavily diluted (and no longer useful for assessing the origins of recently ingested air). Therefore, in the present WRF simulation, we allowed the tracers to freely evolve for 30 min, after which they were reset to their initial concentrations. Within the cyclical 30-min windows, we simply ignore the first  $\sim 10$  min after each reset time. This tracer reset procedure does not impact the fundamental simulation (i.e., the kinematic, thermodynamic, or microphysical fields) in any way.

#### b. Idealized CMI simulation

The “idealized” simulation used version 17 of the CMI model. This simulation used far fewer parameterizations (Table 1), with the intention of providing a simpler framework for physical attribution, and isolating the aspects of the simulated MCS that were self-generated. The initial model environment was horizontally homogeneous and given by a single sounding and wind profile (more on this below). Passive tracers were again added to the initial condition in the lower

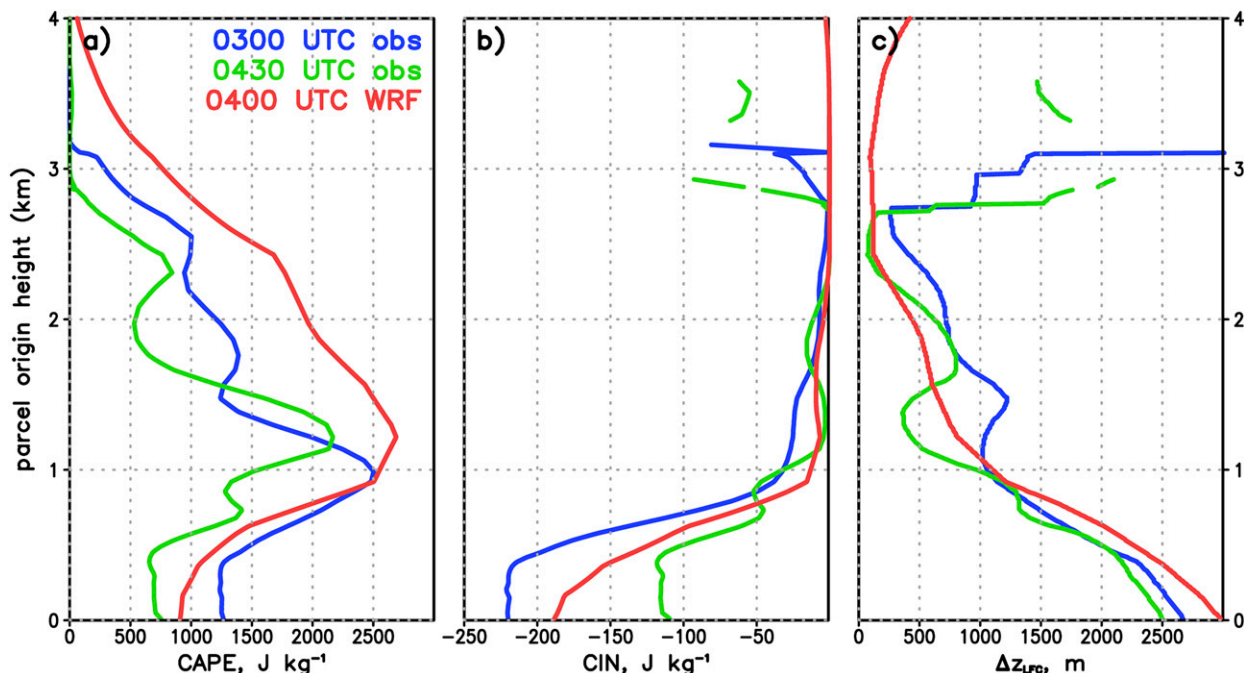


FIG. 3. CAPE, CIN, and required lifting depth ( $\Delta z_{LFC}$ ) as a function of a parcel's original level. CIN and  $\Delta z_{LFC}$  are only plotted for parcels with CAPE  $> 0 \text{ J kg}^{-1}$ . All data from the 0300 UTC 26 Jun 2015 PECAN observation are plotted in blue. All data from the 0430 UTC 26 Jun 2015 PECAN observation are plotted in green. All data from the 0400 UTC WRF Model gridpoint sounding are plotted in red. The original skew  $T$  profiles for these soundings are shown in Fig. 2. The location of the PECAN soundings is indicated in Figs. 1a–b and 4d. The location of the WRF gridpoint sounding is indicated in Figs. 5a, 5b, and 6a.

to midtroposphere (and did not require the periodic resetting used in the WRF simulation).

Whereas the WRF simulation can generate deep convection organically via synoptic and mesoscale processes, the CM1 simulation cannot. Instead, a north–south line<sup>1</sup> of four warm bubbles was introduced into the CM1 model at the initial time, horizontally centered within the model domain; the bubbles had a peak amplitude of 2 K, a horizontal radius of 10 km, and a vertical radius of 1.4 km (centered at 1.4 km AGL). Nevertheless, trial and error revealed that the PECAN soundings taken closest to the observed developing MCS (albeit still  $\sim 100$  km from where it was initiated) did not produce long-lived organized convection in the CM1 model. One possible reason for this is that the CM1

simulation lacks continued destabilization due to ascent<sup>2</sup> from larger-scale forcing. Therefore, the CM1 simulation presented here was initialized with a gridpoint sounding from just ahead of the MCS within the WRF simulation (taken at 0400 UTC; its profile is shown in Fig. 2, and its position is shown in Figs. 5a,b and 6a). Using the WRF gridpoint sounding was a trade-off needed to produce a useful CM1 simulation, but it had the ancillary benefit of making the simulated MCSs in the WRF and CM1 more directly comparable (i.e., the variations between them are not due to differences between the WRF's internal environment and the PECAN soundings).

The rationale for choosing this particular location and time for the WRF gridpoint sounding was the similarity between the WRF's vertical profiles of CAPE, CIN, and required lifting depth ( $\Delta z_{LFC} = z_{LFC} - z_{\text{origin}}$ , i.e., the distance between a parcel's level of free

<sup>1</sup> Readers may wonder why a north–south line of bubbles was used when the observed MCS was initiated along a line running from northeast to southwest (Fig. 1). As shown by the animation in Fig. S1, which includes a simulation initiated with the observed line orientation, the resulting MCS is surprisingly insensitive to this detail. Such robustness adds considerable confidence that the CM1 simulation cleanly embodies self-organizing aspects of an MCS formed in this environment. The north–south trigger was chosen for detailed analysis because it produced less spurious convection in its early stages, and because it tolerated a smaller computational domain for the highest-resolution production runs.

<sup>2</sup> The impacts of this ascent can be seen in the lifting of the thermodynamic profiles between 0300 and 0430 UTC in Fig. 2. Lower tropospheric warm advection (implying quasigeostrophic ascent) is clearly present (e.g., veering of the wind with height in Fig. 2), and the observational analyses of Miller et al. (2019) document substantial isentropic upglide within the frontal zone, having kinematic vertical velocities approaching  $0.2 \text{ m s}^{-1}$ .

TABLE 1. Summary of model settings for the WRF (v. 3.6) and CM1 (v. 17) simulations in this article. The colloquial names for various parameterizations are given in the table, with corresponding literature citations as follows: Thompson scheme (Thompson et al. 2008); Morrison scheme (Morrison et al. 2009); MYJ boundary layer scheme (Mellor and Yamada 1982; Janjić 2002); TKE-based subgrid closure (Deardorff 1980; Bryan and Morrison 2012); RRTM–Dudhia scheme (Mlawer et al. 1997; Dudhia 1989); Noah–Eta scheme (Chen and Dudhia 2001); Kain–Fritsch scheme (Kain and Fritsch 1993; Kain 2004).

Setting	WRF simulation	CM1 simulation
$\Delta x, \Delta y$	15–3–1 km, two-way nested 0.33 km, one-way nested	0.25 km
Vertical levels	d01, d02, d03: 40 d04: 79	72
$\Delta z$	d01, d02, d03: stretched, $\approx 50$ –660 m d04: stretched, $\approx 25$ –330 m	Stretched, 100–250 m
Model top	$\approx 20.5$ km	16.5 km
Microphysical parameterization	Thompson scheme	Morrison scheme
Turbulence parameterization	MYJ boundary layer scheme	TKE-based subgrid closure
Radiation parameterization	RRTM–Dudhia scheme	None
Land–surface parameterization	Noah–Eta scheme	None, free-slip bottom boundary
Convective parameterization	Kain–Fritsch scheme (15-km nest only)	None
Initialization	NAM model analysis 0000 UTC 25 Jun 2015	Horizontally homogeneous with inserted line of 4 warm bubbles
Lateral boundary conditions	NAM model analyses every 6 h	Open radiative condition
Simulation time	Ending time 0900 UTC 26 Jun 2015 d01 33 h, d02 15 h, d03 9 h, d04 9 h	6 h
Dynamical simplifications	None	Coriolis acceleration omitted

convection, or “LFC”, and its origin height) as compared to the 0300 and 0430 UTC observed soundings (Fig. 3). Much like the 0430 UTC observed profile, the 0400 UTC WRF point sounding is close enough to the MCS that there is some evidence of upper-tropospheric modifications (e.g., the upper-level warming, moistening, and enhanced westerlies are consistent with a leading anvil); these modifications produce somewhat lower CAPE values and higher deep-layer shear values than in the undisturbed environment. Even so, of primary importance is the overall similarity of the 0400 UTC WRF thermodynamic profiles to the 0430 UTC observed profiles in the lowest 1 km AGL (up to roughly 850 hPa; Fig. 2). Thereabove, the WRF profile has marginally higher humidity and steeper lapse rates (yielding more CAPE and slightly smaller  $\Delta z_{\text{LFC}}$  there; Fig. 3). Relative to the observed soundings, this would presumably make the WRF environment (and subsequent CM1 environment using its point sounding) somewhat more favorable for the development and maintenance of elevated convection. The basic metrics for surface-based convection in the WRF environment are neither more nor less favorable than the observations, although it is possible that slightly stronger elevated convection (due to higher CAPE aloft) could subsequently enhance surface cold pool development. The WRF environment also has a slightly longer low-level hodograph (Fig. 2), which increased the 0–3-km environmental helicity slightly (from 402 to 418  $\text{m}^2 \text{s}^{-2}$ ) and the 0–3-km storm-relative helicity more

substantially (from 646 to 757  $\text{m}^2 \text{s}^{-2}$ , using the observed MCS’s motion) in comparison to the 0430 UTC observed wind profile. This might make the WRF environment somewhat more favorable for the production of embedded mesovortices, a point that is discussed further in section 5.

In addition to such local comparisons, it is also worth quantifying the variability of the background environment from which the gridpoint sounding was taken. As shown in Fig. 5, the MCS was initially moving east-southeastward into a corridor with rather uniform values of surface-based (SB) and most-unstable (MU) parcel CAPE and CIN. In general, the 0400 UTC pre-MCS environment in the WRF simulation had moderate SBCAPE with considerable SBCIN, and high MUCAPE with minimal MUCIN, much as was observed (Fig. 3). Beyond the modest initial gradients in instability ahead of the MCS, the observed MCS would naturally experience temporal evolution of its environment. The passage of time during the overnight hours tended to decrease CAPE values (cf. top and bottom rows of Fig. 5) but this was offset by the MCS’s tendency to move toward the surface front over time (e.g., as shown in Fig. 1). Overall, the parameters immediately ahead of the MCS therefore changed less over time than might otherwise be anticipated (i.e., the pre-MCS values at both times in Fig. 5).

### 3. Overview of observed case and simulations

During the overnight hours of 24–25 June 2015, a surface front slowly moved southward across the central

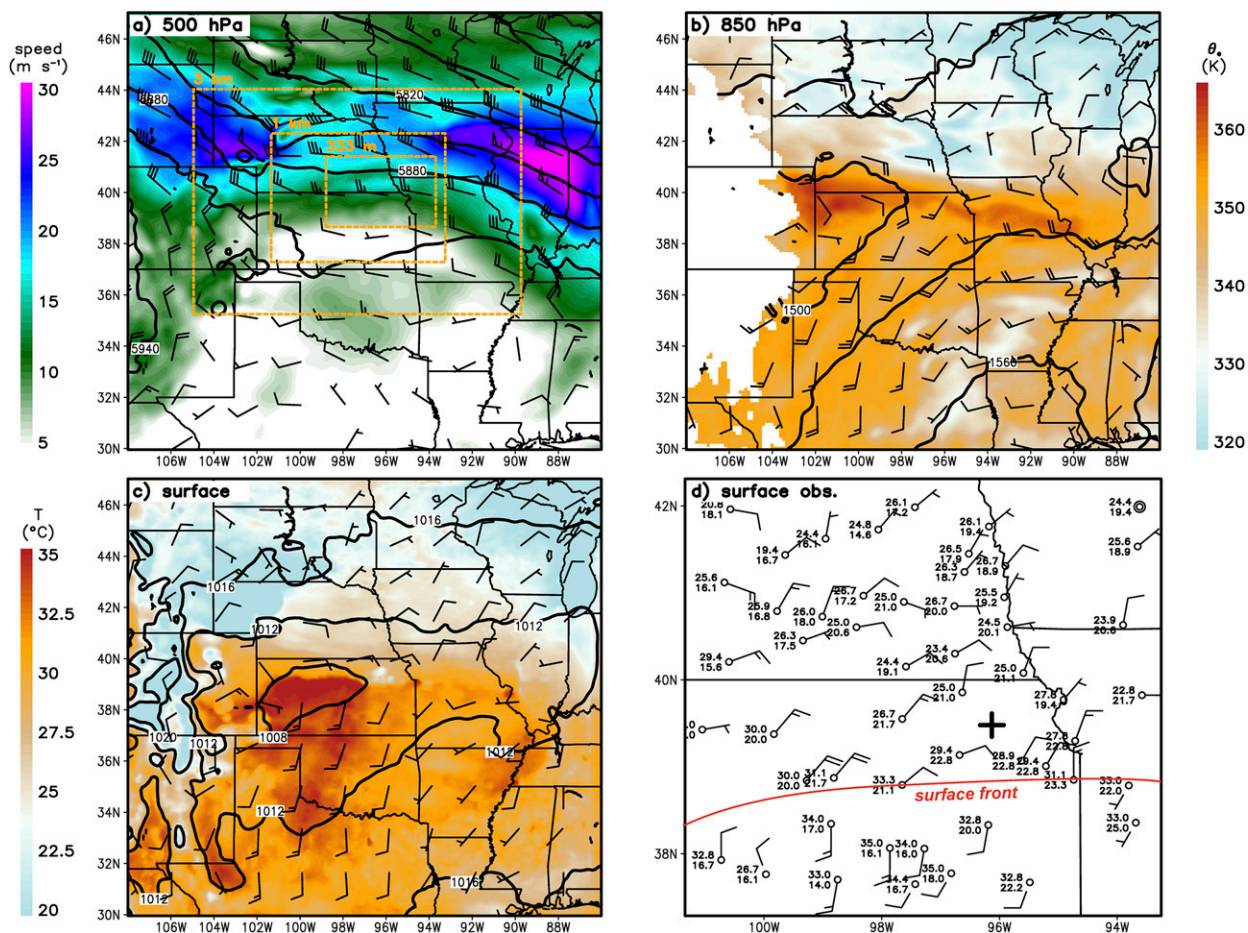


FIG. 4. Synoptic overview at 0000 UTC 26 Jun 2015: (a) 500 hPa heights (contoured in m), wind barsbs (barb = 5 m s<sup>-1</sup>, flag = 25 m s<sup>-1</sup>), and isotachs (shaded in m s<sup>-1</sup>); (b) 850 hPa heights (contoured in m), wind barsbs (barb = 5 m s<sup>-1</sup>), and equivalent potential temperature ( $\theta_e$ , shaded in K); (c) surface pressure reduced to mean sea level (contoured in hPa), wind barsbs (barb = 5 m s<sup>-1</sup>), and temperature (shaded in °C); (d) standard station model plot of observed surface temperature (°C), dewpoint temperature (°C), and wind barsbs (barb = 5 m s<sup>-1</sup>). Data in (a)–(c) are from the outermost domain (15-km grid spacing) of the WRF simulation described in this study. Data in (d) are standard hourly surface observations. The extents of the WRF nested grids (3-km, 1-km, and 333-m grid spacing) are indicated in (a). The location of the primary surface front at each hour is annotated in (d), with a black cross indicating the location of the 0300 UTC and 0430 UTC observed soundings from PECAN (Figs. 2 and 3).

Great Plains, passing through southern Nebraska and stalling in northern Kansas during the day on 25 June (not shown). As of 0000 UTC 26 June, an upper-tropospheric short-wave trough and jet streak were moving southeastward toward central Nebraska (Fig. 4a), with an associated surface low pressure center occurring over the High Plains of western Kansas (Fig. 4c). A stationary front remained across northern Kansas, with a rather sharp wind shift and a temperature difference of roughly 5°C across the boundary (Figs. 4c,d). On the poleward side of the front, along the Nebraska–Kansas border, a mesoscale maximum in equivalent potential temperature ( $\theta_e$ ) was evident above the surface at 850 hPa (Fig. 4b), which was reflected in the

PECAN soundings released in that region (Fig. 2; the sounding location relative to the surface front is shown in Fig. 4d). With 10–15 kt (5–8 m s<sup>-1</sup>) southerly warm sector surface winds and 15–25 kt (8–13 m s<sup>-1</sup>) southerly 850 hPa winds yielding upgliding motion in the vicinity of the stationary front (Figs. 4b–d), the setting was quite favorable for the development of elevated, post-frontal convection.

Between 0200 and 0300 UTC 26 June, deep convection developed in the zone of frontal upglide, roughly 100–150 km north of the surface front (Fig. 1a). The environment sampled by PECAN soundings at 0300 UTC (shortly after, but somewhat southeast of, convective initiation) had SBCAPE exceeding 1000 J kg<sup>-1</sup> but

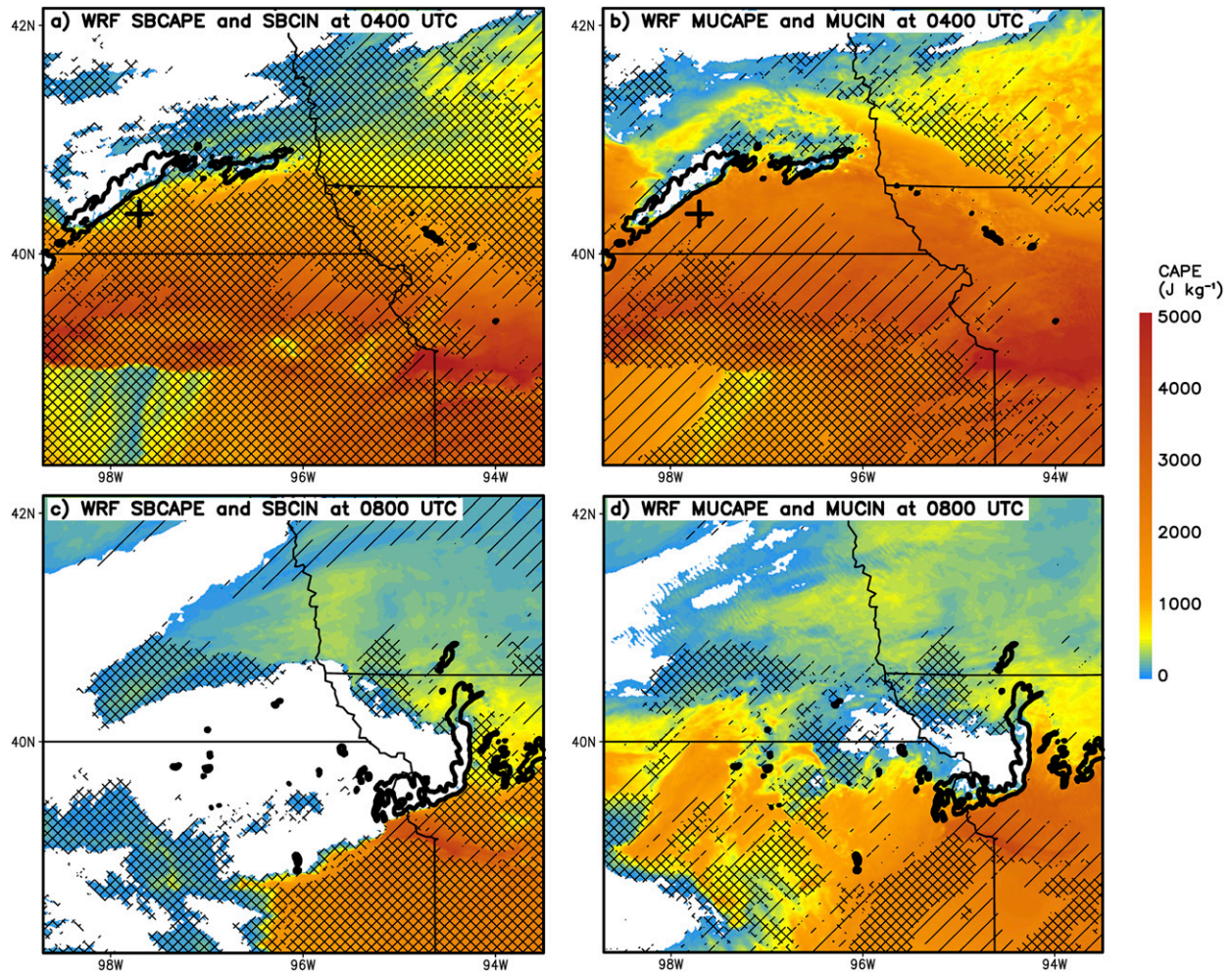


FIG. 5. (a),(b) CAPE and CIN from the WRF simulation at 0400 UTC and (c),(d) at 0800 UTC. In (a),(c), CAPE and CIN are plotted for the surface-based (SB) parcel. In (b),(d), CAPE and CIN are plotted for the most unstable (MU) parcel in the profile. In all panels, CAPE is shaded as shown in  $\text{J kg}^{-1}$  and CIN is represented with hatching:  $-50$  to  $0 \text{ J kg}^{-1}$  is unhatched,  $-100$  to  $-50 \text{ J kg}^{-1}$  has sparse single hatching, beyond  $-100 \text{ J kg}^{-1}$  has dense double hatching. The thick black contour in each panel shows the MCS's 45 dBZ simulated reflectivity contour at the same time. The location of the WRF gridpoint sounding (profiles in Figs. 2 and 3) is indicated with a cross in (a),(b).

with SBCIN of approximately  $-220 \text{ J kg}^{-1}$  (Figs. 3a,b, blue profiles). These surface parcels would hypothetically require lifting in excess of 2.5 km in order to reach their levels of free convection (LFCs; Fig. 3c, blue profile). However, the most unstable parcels resided roughly 1 km AGL, with CAPE of approximately  $2500 \text{ J kg}^{-1}$ , CIN of approximately  $-30 \text{ J kg}^{-1}$ , and  $\Delta z_{\text{LFC}}$  of approximately 1.0 km (Fig. 3, blue profiles). Even farther aloft, air parcels had less overall CAPE but also possessed negligible CIN and an even smaller  $\Delta z_{\text{LFC}}$  (Fig. 3, blue profiles). A later 0430 UTC PECAN sounding (located much closer to the approaching MCS) exhibited low-level cooling and moistening consistent with ascent below 700 hPa (Fig. 2), much as was diagnosed in the detailed observational study of Miller

et al. (2019). This ascent resulted in reduced CAPE but also reduced CIN through most of the lower troposphere (Fig. 3, green profiles). Altogether, this environment would appear to have readily supported elevated convection based in a rather broad layer aloft; in contrast, very deep and intense near-surface lifting would be required to initiate and maintain surface-based convection.

The group of storms was initially somewhat linearly oriented and very quickly acquired a classic QLCS structure, including an emerging region of trailing stratiform precipitation, as it approached the PECAN field assets between 0400 and 0500 UTC (Figs. 1b,c). Not a single severe surface wind report occurred during the first  $\approx 3$  h of the MCS's life

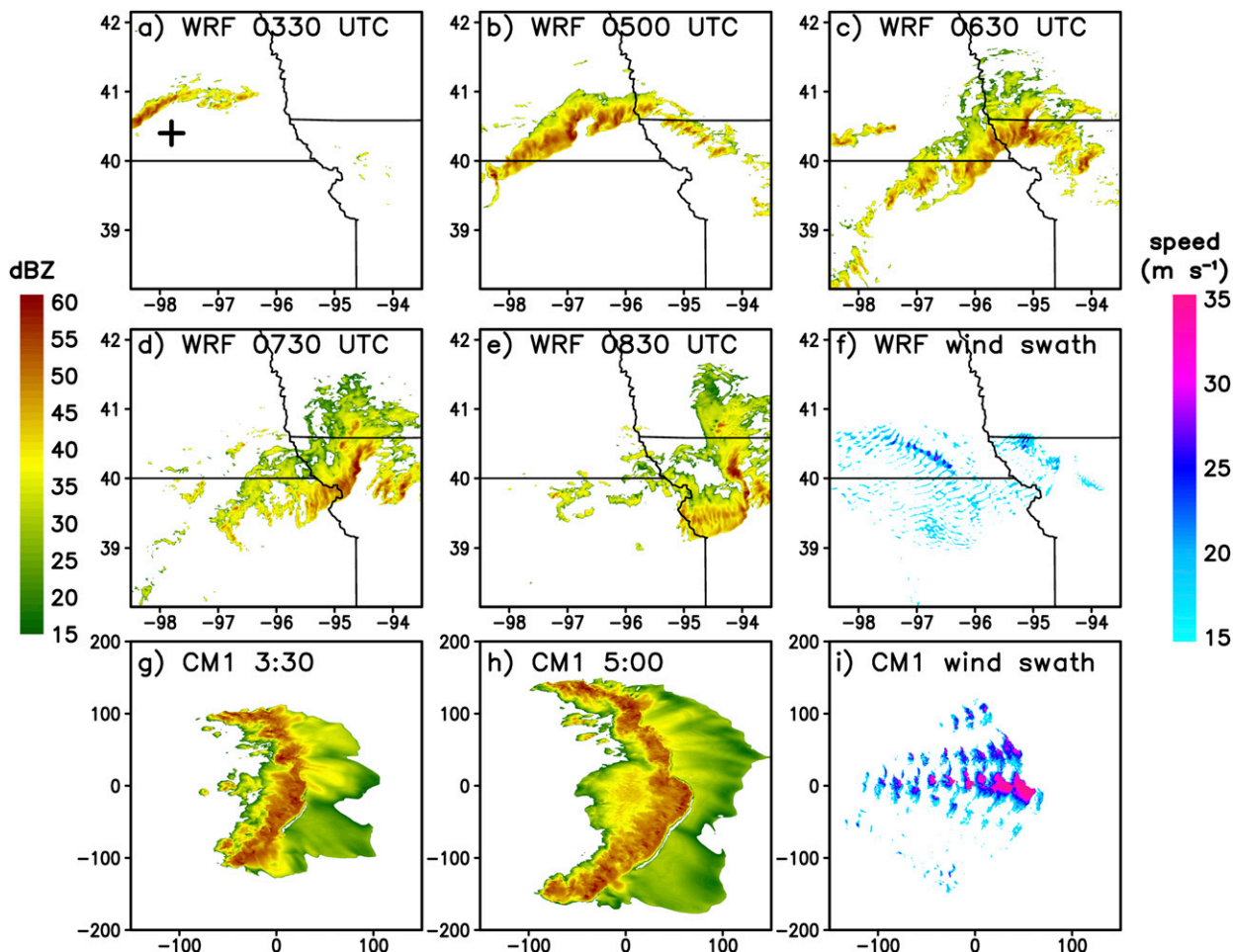


FIG. 6. (a)–(e),(g),(h) Simulated logarithmic radar reflectivity factor (dBZ) and (f),(i) simulation-maximum ground-relative winds ( $m s^{-1}$ ) at the surface from the 1-km domain of the (a)–(f) WRF simulation and from the (g)–(i) CM1 simulation. WRF simulations are labeled in UTC with latitude–longitude tick marks, whereas CM1 simulations are labeled by elapsed time, with tick marks in km. Surface winds are shaded using the color scale at right; logarithmic reflectivity factor is shaded using the color scale at left. The WRF wind swath uses the magnitude of the simulated 10 m wind with a 10-min interval. The CM1 wind swath uses the  $u$  component at the bottom model level, translated by adding on the domain’s motion, with a 20-min interval. Animated renderings of these panels are given in Figs. S2 (for WRF) and S3 (for CM1).

(Fig. 1); prior to 0500 UTC, peak 1-s surface winds of 12–15  $m s^{-1}$  were observed by the five PECAN mobile surface stations within the convective region and developing cold pool. Despite a continued lack of PECAN-measured surface winds  $\geq 26 m s^{-1}$ , an initial severe wind report (tree damage) occurred in Kansas at 0521 UTC, in association with a small-scale embedded bowing segment (Fig. 1d). A more sustained period of severe winds began with a report at 0607 UTC, after which time at least one report was received during each 10-min period through 0730 UTC (Figs. 1e,f). As noted by Miller et al. (2019), by this time the MCS was located considerably closer to the surface front’s position (e.g., Fig. 1e), such that the depth of the postfrontal stable layer was likely shallower

than what the MCS experienced earlier in its lifetime. The MCS continued to produce severe wind reports in Missouri through 0917 UTC (not shown), becoming more sparse after the system exited the Kansas City metropolitan area. Although severe winds are typically under-reported at night (Trapp et al. 2006), and there is likely a population bias associated with (earlier) rural versus (later) urban impacted locations, five measured severe wind gusts occurred starting at 0642 UTC, while neither PECAN assets nor operational surface stations recorded any severe winds prior to then.

The multi-Doppler radar wind syntheses of Miller et al. (2019) support the development of an increasingly strong and distinct zone of lower tropospheric

outflow by roughly 0430–0500 UTC. Their analysis of mesonet stations also shows that, by this 0430–0500 UTC window, the passage of the MCS was accompanied by a surface wind shift and roughly 3–5 K temperature decline. Together, these measurements imply the existence of a surface cold pool and gust front. Although the required vertical displacements for surface-based convection remained roughly 2.5 km as of the 0430 UTC PECAN sounding (Fig. 3c, green profile), the surface cold pool inferred from Miller (2018)'s diabatic Lagrangian analyses far exceeded this depth by 0500 UTC. In keeping with the hypothesized transition to surface-based convection, Miller et al. (2019)'s multi-Doppler syntheses support that streamlines entered the MCS's updrafts from progressively lower altitudes over time. Unfortunately, the MCS began its most prolific severe wind production as it exited the PECAN measurement domain studied by Miller et al. (2019). The present simulations help to assess the relevant processes both during and after the purported transition from an elevated to a surface-based, severe wind-producing QLCS.

In the WRF simulation, convection was initiated slightly later and farther to the northwest than in reality (cf. Figs. 1a,b vs Figs. 6a,b). Such differences are not surprising; as noted by Peters et al. (2017), even small thermodynamic errors can lead to position differences of 100–200 km when convection is formed in zones of gradual frontal upglide. Notwithstanding these initial displacements and a somewhat smaller trailing stratiform rain area, the evolution of the WRF simulated convection over the subsequent 5 h is quite reminiscent of the observed system (cf. Figs. 1b–f vs Figs. 6b–f). Convection progressively develops into a southeastward-moving QLCS with embedded bowing segments (Figs. 6c–e, and animated depiction in Fig. S2 in the online supplemental material). Both the observed and simulated systems produce swaths of severe surface winds during the 0600–0830 UTC period (Figs. 1d–f and 6f). It is notable that the WRF simulation produces severe winds earlier in the simulation as well (in southeastern Nebraska), which may mean that its cold pool production and transition toward surface-based convection are somewhat accelerated compared to the observed MCS; the details of this evolution and severe wind production are examined more in sections 4 and 5.

The idealized CM1 simulation captures a number of key aspects of the observed MCS, including a convective line extending from southwest to northeast that has embedded bowing segments producing severe surface winds (Figs. 6g–i, and animated depiction in Fig. S3). The degree of idealization in the CM1

simulation leads to a few discrepancies,<sup>3</sup> including a line segment that extends well to the northwest. This spurious part of the simulated MCS exists because (unlike in nature and in the WRF simulation) the lower troposphere does not become cooler and more stable as one moves northward within the CM1's homogeneous environment; for this reason, we will not analyze the northern flank of the MCS in the present article. The surface winds produced in the CM1 simulation (Fig. 6i) also exceed those in the WRF simulation (Fig. 6f), and possibly those in nature (although 0.5° elevation radar radial velocities were observed to exceed 40 m s<sup>-1</sup>; interested readers may look ahead to Fig. 16). This is likely attributable to the lack of surface drag and the omission of a PBL parameterization in the CM1 simulation (plus its higher resolution than the WRF simulation); nevertheless, the severe winds occur at roughly the same position and time in the WRF and CM1 MCSs' life cycles.

In both simulations, progressively stronger surface winds (Fig. 7a) and colder outflow (Fig. 7b) occur through the first several simulated hours. Ultimately, in both cases the simulated convection consistently exceeds the threshold for severe thunderstorm winds after several hours. The cold pool strengths are quite similar in the WRF and CM1 simulations, with peak temperature deficits of 6–7 K (Fig. 7b). While these simulated deficits exceed those from the PECAN observing area (generally around 3 K, as summarized by Miller et al. 2019), temperature drops of 5–6 K were subsequently observed to the immediate southeast at the Topeka and Lawrence, Kansas, ASOS sites around 0600 UTC, with a later decrease as large as 8 K observed at the Kansas City, Missouri, downtown airport when the MCS was at its most intense (around 0700 UTC). The simulated strengthening of the cold pool in both models is also contemporaneous with a transition toward surface-based

<sup>3</sup> Another unique feature of the CM1 simulation is a region of "leading stratiform" precipitation that precedes the eastward-moving convective line. Previous work by Parker and Johnson (2004a,b) suggests that such structures are not uncommon in environments with strong upper-tropospheric vertical wind shear, as can be seen in the 500–200 hPa layer in the present case (Fig. 2). There is indeed evidence of leading stratiform precipitation above 4 km AGL in the radar observations of the 25–26 June MCS (not shown), however this precipitation apparently did not reach the surface in reality. In the authors' experience, small regions of precipitation descending to the surface downstream of simulated convection are not uncommon when the Morrison et al. (2009) microphysics parameterization is used in strongly sheared environments. In this case, the leading stratiform region is probably enhanced by using the preline WRF point sounding that, much like the 0430 UTC observed sounding, has already undergone considerable moistening aloft (Fig. 2).

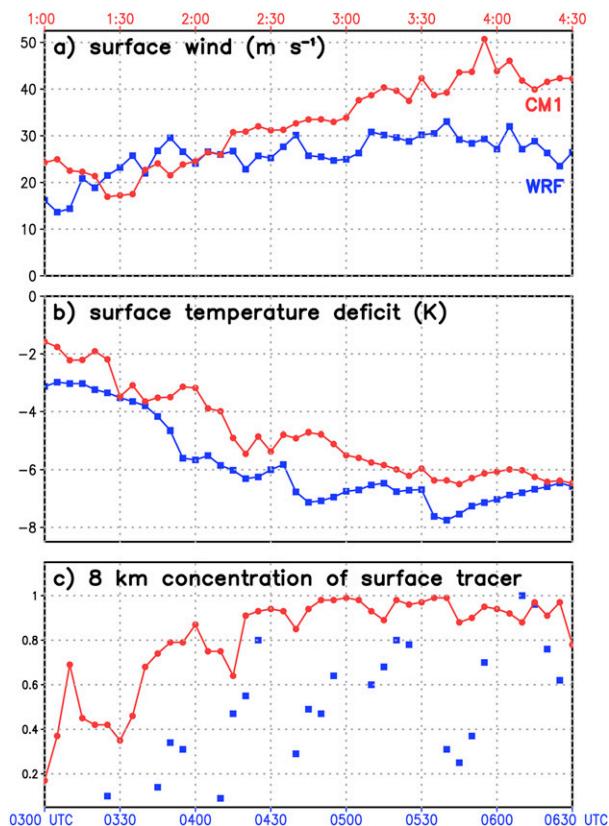


FIG. 7. History of (a) maximum surface winds, (b) maximum surface cold pool temperature deficit, and (c) maximum concentration of the 0–500-m tracer found at 8 km AGL, from the 333-m domain of the WRF simulation (blue) and from the CM1 simulation (red). WRF simulations are labeled by UTC (bottom/blue abscissa), whereas CM1 simulations are labeled by elapsed time (top/red abscissa). Maxima for the WRF simulation are for a 100 km × 150 km area following the most intense part of the MCS (to remove spurious values related to far field heterogeneity); maxima for the CM1 simulation are for the entire model grid. The WRF surface winds are the magnitude of the simulated 10 m wind; the CM1 surface winds are the *u* component only, adjusted to ground-relative by adding on the domain’s motion. The WRF tracer time series is masked for the first 10 min after each half hourly cycle at which the tracer was reset to its initial value (explained in section 2a).

convection, as demonstrated by the increasing concentration of near-surface tracer that is found in the upper troposphere (Fig. 7c). The CM1 simulation has higher tracer concentrations aloft than the WRF simulation because it does not use a PBL parameterization, the effect of which is to diffuse the tracer in low levels (thereby decreasing values in the surface-based updrafts); to overcome this issue in the WRF simulation, the tracer is reset at half-hour intervals (as explained in section 2a), but this also prevents the WRF simulation from accumulating high concentrations of surface tracer aloft.

The pair of simulations were undertaken at very different levels of complexity, and unsurprisingly they

differ in their details. Even so, both the WRF and CM1 experiments support the narrative of an MCS that initially comprises primarily elevated convection, but later develops a surface cold pool and simultaneously begins producing severe surface winds and lifting surface air into the upper troposphere within its updrafts. The WRF simulation is a credible representation of the MCS in its synoptic and mesoscale settings, notwithstanding its position errors. Meanwhile, the horizontally homogeneous CM1 simulation produces an MCS with a spurious northern extension of its convective line, but reasonably represents the self-organizing aspects of an MCS in this environment. As a pair, the simulations can be used as a basis for the kinds of analysis that observations alone would not permit. The focus of the remainder of this article is on the key processes during the window of time in which the simulated MCSs transition from elevated to surface-based convection (section 4), and on the mechanisms responsible for their period of most prolific severe surface wind production (section 5).

#### 4. Evolution from elevated to surface-based convection

To understand the transition of the MCS from elevated to surface based, we begin with the fundamental requirement that air from near the ground must be lifted to its LFC in order to take part in the convective updrafts. As shown in Fig. 3c, the required vertical displacement for surface air is at least 2.5 km, and in the models’ initial environments (red profile) is closer to 3.0 km. The most likely mechanisms for providing such deep lifting in MCSs are system-generated surface cold pools, some of which have been observed to exceed 4 km in depth (Bryan and Parker 2010; Hitchcock et al. 2019). This hypothesis fits with the correspondence in time between the temperature of the surface outflow and the presence of surface tracer in deep updrafts (Figs. 7b,c), so we examine it further.

In the early stages of both simulations, the low-level air is generally not being lifted into the mid- and upper levels (5–10-km tracer concentrations shown by cyan contours in Figs. 8a,c). The lack of initial cold pool development is represented by the largely undisturbed surface tracer field at the bottom model level in both runs (shaded in Figs. 8a,c). This corresponds to the “underflow” state described by Parker (2008), in which surface air simply passes beneath elevated convective updrafts aloft. As of  $t = 0130$  in the CM1 simulation, a very weak surface cold pool is evident (near  $x = 70$  km in Figs. 9c,d), but with minimal vertical displacement of the surface tracer (and thus a midlevel updraft that is completely devoid of surface air; Fig. 9b).

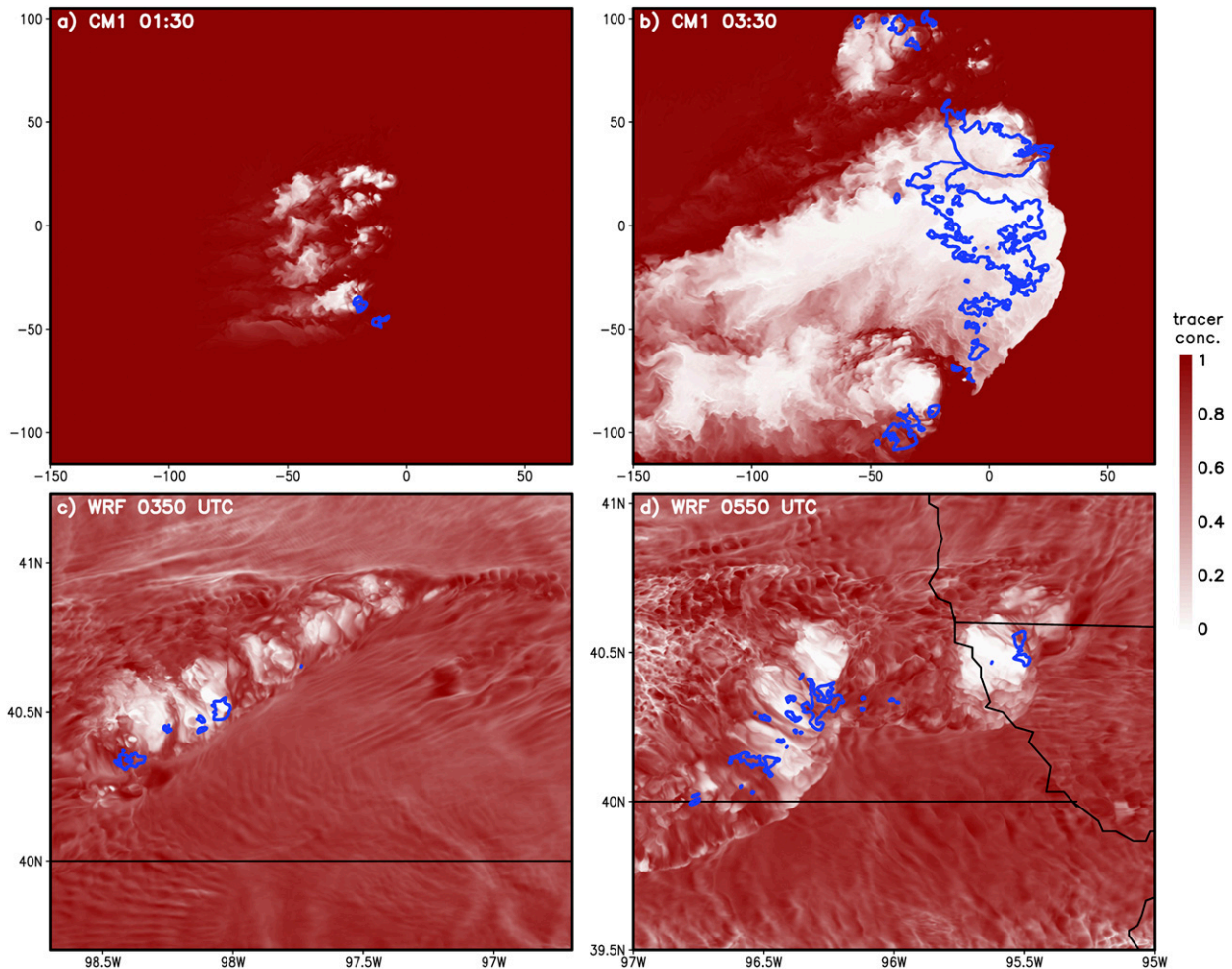


FIG. 8. Simulated concentration of the (unitless) tracer introduced in the 0–500 m AGL layer, plotted at the surface (shaded as shown) and as a column maximum in the 5–10 km AGL layer (contoured in blue at a concentration of 0.20). (a),(b) CM1 simulation (at run times of 0130 and 0330, respectively); (c),(d) WRF simulation (at simulated times of 0350 UTC and 0550 UTC, respectively). Each of the WRF depictions occurs 20 min after the tracer reset procedure described in section 2a.

A domelike structure is evident in the potential temperature surfaces in the layer 1–3 km AGL (leading edge at  $x^* \approx 65$  km in Figs. 9c,d), which in some respects resembles the bore structures studied by Parker (2008), in which a surface cold pool formed early on and subsequently impinged on a stable layer. However, here this structure originates prior to the development of a prolific surface density current (thus more closely resembling the studies of Schmidt and Cotton 1990; Schumacher and Johnson 2008; Schumacher 2009; Marsham et al. 2010, 2011). In the present simulations, the deepening of the stable layer originates from enhanced near-ground convergence arising in response to convective heating aloft (as in Schumacher and Johnson 2008; Schumacher 2009). In time, a quasi-static pressure maximum emerges beneath the deepened part of the stable layer, and it is progressively

reinforced by hydrometeor loading and evaporative cooling associated with the deep convection. The resulting depth, pressure, and wind perturbations have gravity wave phase relationships that sustain the persistent domelike structure. To avoid confusion with classical bores, we will generically refer to this feature as a wavelike disturbance. This disturbance is what continues to lift elevated parcels to their LFCs. The vertical displacements required to support free convection are quite small for most of the air parcels in the 1–3-km layer (Fig. 3c), so the wavelike disturbance suffices for self-maintenance of the MCS in CM1 (until sufficiently widespread convection can potentially build up a surface cold pool).

In the WRF simulation, things have progressed a bit farther by the time of the 0350 UTC cross section (Fig. 10), and a roughly 0.5-km-deep surface cold pool

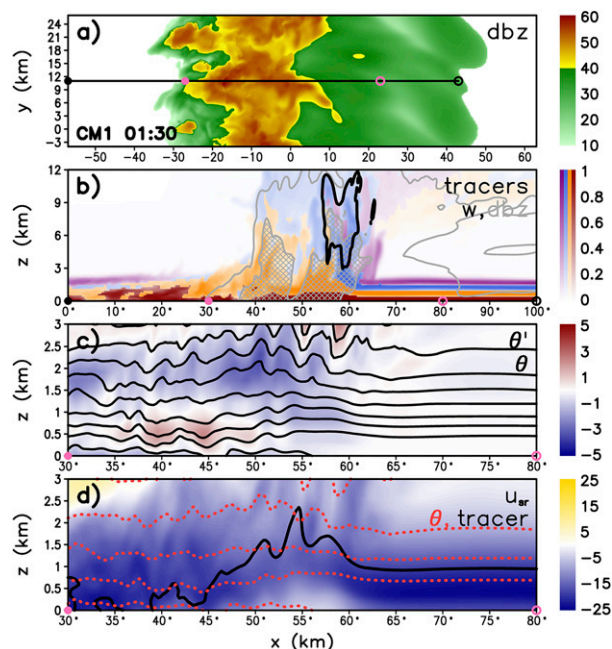


FIG. 9. Depiction of selected fields at  $t = 0130$  from the CM1 simulation: (a) plan view of simulated logarithmic radar reflectivity factor at the bottom model level (dBZ, shaded); (b) vertical cross section of passive tracer concentrations originating from four layers (shaded by the tracer with the greatest concentration in each grid cell, with 0.0–0.5 km in red, 0.5–1.0 km in orange, 1.0–1.5 km in blue, 1.5–2.0 km in purple), with vertical velocity contoured in black at  $10 \text{ m s}^{-1}$  and logarithmic radar reflectivity factor contoured in gray at 25 dBZ and hatched above 50 dBZ; (c) vertical cross section of potential temperature perturbation (K, shaded) and potential temperature (contoured every 2 K); (d) vertical cross section of storm-relative  $u$  wind ( $\text{m s}^{-1}$ , shaded), potential temperature (contoured in red every 4 K), and concentration of tracer originating below 1 km AGL (contoured in black at 0.6). The horizontal positions of the vertical cross sections are shown via the black line segment and black/pink circles in (a). All fields in the vertical cross sections are averaged over a 5-km-wide horizontal swath that is centered on this line. All axis labels are in km; the  $x$ -axis values in (a) are for the native model grid, whereas the  $x$ -axis labels in (b)–(d) are distance along the cross section. To show detail, the horizontal and vertical axes are zoomed in (c),(d).

is evident (Figs. 10c,d) along with at least some vertical displacement of the surface tracer (Fig. 10a). Notably, however, there is still evidence of tracer “underflow” in the WRF (black contour in Fig. 10d), the midlevel updraft is still devoid of surface air (Fig. 10b), and a wavelike disturbance is pronounced in the 1–3 km AGL layer (Fig. 10c). A plan view of the tracer field (Fig. 8c) reveals that only very small pockets of penetrative downdrafts and lofting of surface air are present at 0350 UTC; the cross section in Fig. 10 is taken through one of the line’s most intense portions.

Advancing by 2 h in both simulations, a greater concentration of low-level air is found aloft in the 5–10 km

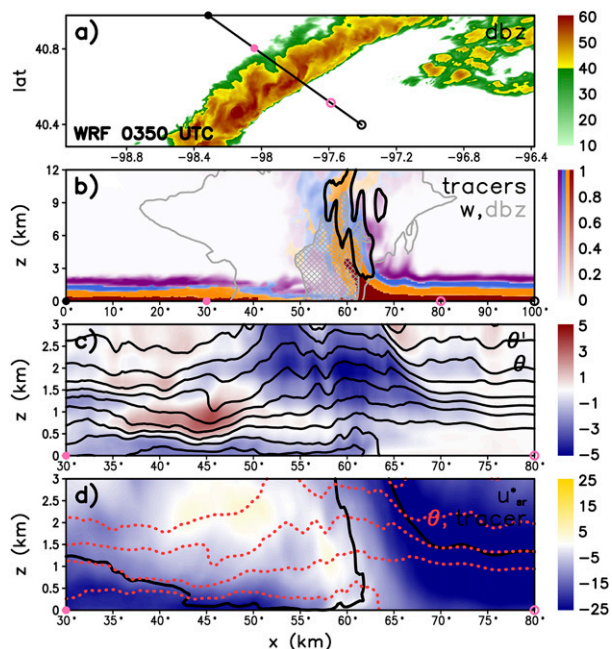


FIG. 10. As in Fig. 9, but from the WRF simulation at  $t = 0350$  UTC. The axis labels in (a) are longitude–latitude, whereas the  $x$ -axis labels in (b)–(d) are distance along the cross section. In (d), the storm-relative wind’s tangential component (within the cross section) is shown rather than the  $u$  wind (as in Fig. 9d).

AGL layer (cyan contours in Figs. 8b,d). The maturation of surface cold pools is indicated by the widespread pockets wherein the 0–500-m tracer has been displaced (low values shaded in Figs. 8b,d). This indicates that the previous “underflow” condition has been replaced by a regime in which midlevel air is descending to the surface (this is further demonstrated in a moment) and low-level air is being lifted at the system’s leading edge. In the CM1 simulation at  $t = 0330$ , a surface cold pool approaching 1 km in depth exists (assessed as the peak height of the environmental surface potential temperature contour; Figs. 11c,d), with upward displacement of the surface tracer occurring at the outflow boundary and extending to midlevels within convective updrafts (Fig. 11b). In many respects, this mature system resembles a classical surface-based, cold pool–driven squall line such as might be observed under afternoon conditions. The primary distinction is the continued presence of the wavelike disturbance that is present in the ambient stable layer, which remains roughly collocated with the leading edge of the surface outflow. As a result, the updraft continues to include a significant amount of elevated air (non-red tracers in Fig. 11b), indicating that parcels within a deep layer are being lifted to their LFCs. The cross sections through the WRF MCS at 0550 UTC paint a similar picture (Fig. 12).

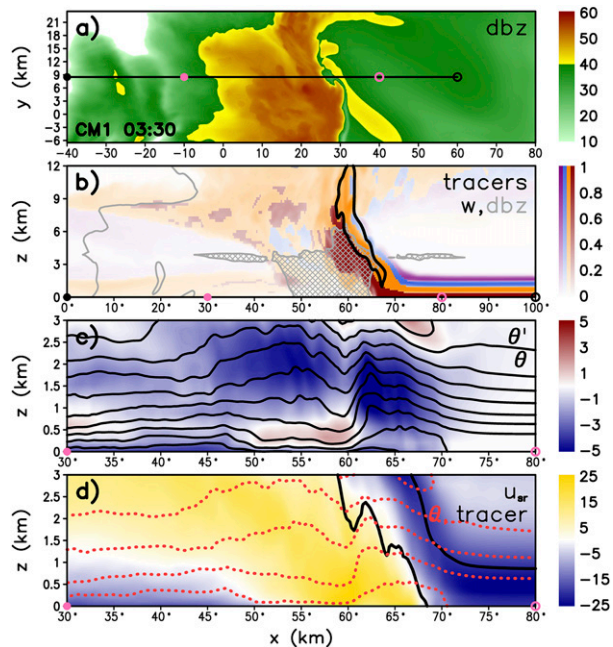


FIG. 11. As in Fig. 9, but from the CM1 simulation at  $t = 0330$ .

As before, the WRF surface cold pool is slightly stronger than in CM1, and the tracers are also considerably more diffused (this is also due to the continuing action of the model's boundary layer parameterization).

At this point, the top of the wavelike disturbance approaches 4 km AGL in both the CM1 and WRF simulations, implying that an extremely deep layer of pre-MCS air is being lifted as it approaches the leading edge of the system. Even so, much like at the earlier times, the development of the surface cold pool seems to be horizontally heterogeneous in both models (Figs. 8b,d), with pockets of relatively undisturbed surface air interspersed within the broader envelope of surface outflow. In both models the simulated MCS nevertheless has a rather uniform leading edge (e.g., Fig. 6), which implies that QLCS structures in radar imagery may not uniquely correspond to one single forcing mechanism (e.g., a cold pool, a bore, or a gravity wave).

The transition of the MCS from elevated convection to (at least partially) surface-based convection seems to be linked to the development of the surface cold pool. Thus, its genesis and properties are of great interest. The nearly saturated state of the soundings representing the preconvective environment in both models (red curve in Fig. 2) would not appear to support substantial evaporative cooling in the lowest  $\approx 3$  km AGL. In turn, the absence of surface tracer (Fig. 8) in what cross sections reveal to be surface cold pools (Figs. 11 and 12) implies that the source of air within the cold pool must be from aloft. Whereas the

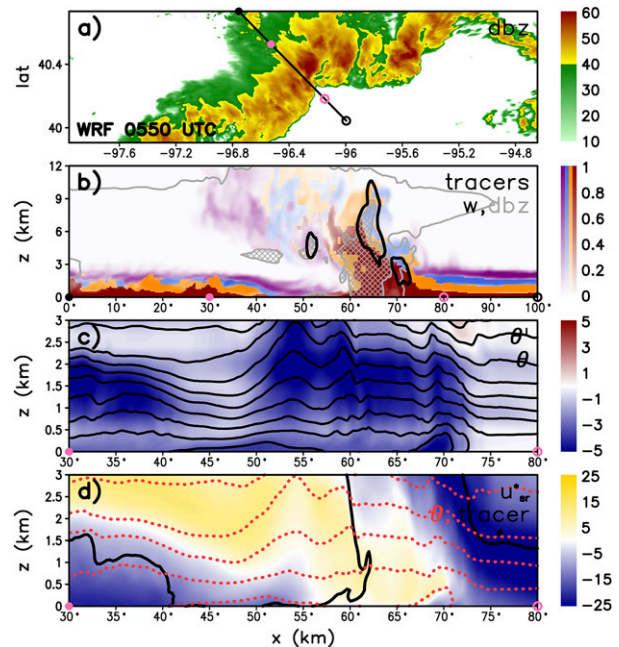


FIG. 12. As in Fig. 9, but from the WRF simulation at  $t = 0550$  UTC. The axis labels in (a) are longitude–latitude, whereas the  $x$ -axis labels in (b)–(d) are distance along the cross section. In (d), the storm-relative wind's tangential component (within the cross section) is shown rather than the  $u$  wind (as in Fig. 9d).

ambient environmental surface air in the homogeneous CM1 simulation has  $\theta_e \approx 347$  K (Fig. 13a), the developing surface cold pools exhibit much lower values, in places falling below 330 K (e.g., Fig. 13b). If  $\theta_e$  is approximately conserved, such air would appear to originate from 4 to 6 km AGL in this environment; the cross sections constructed from PECAN soundings by Miller et al. (2019) similarly support a source of cold pool air from above 3 km AGL (Fig. 13c), and that essentially all of the cold pool contains at least some air from above 3 km AGL (Fig. 13d).

In the WRF simulation, midlevel tracers are less helpful owing to our recurring tracer reset procedure as well as diffusion imparted by the PBL parameterization. Nevertheless, values of  $\theta_e < 335$  K are widespread within the cold pools (Fig. 14); such low values are found only above 3 km AGL in both the pre-MCS and post-MCS vertical profiles (Fig. 14a). This pathway (cooling and descent of low  $\theta_e$  air from aloft) is reminiscent of the zone of descending rear inflow air that occurs in classical squall lines with regions of trailing stratiform precipitation (e.g., Newton 1950; Zipser 1977; Smull and Houze 1987; Bryan and Parker 2010). In both the CM1 and WRF simulations, this corridor of

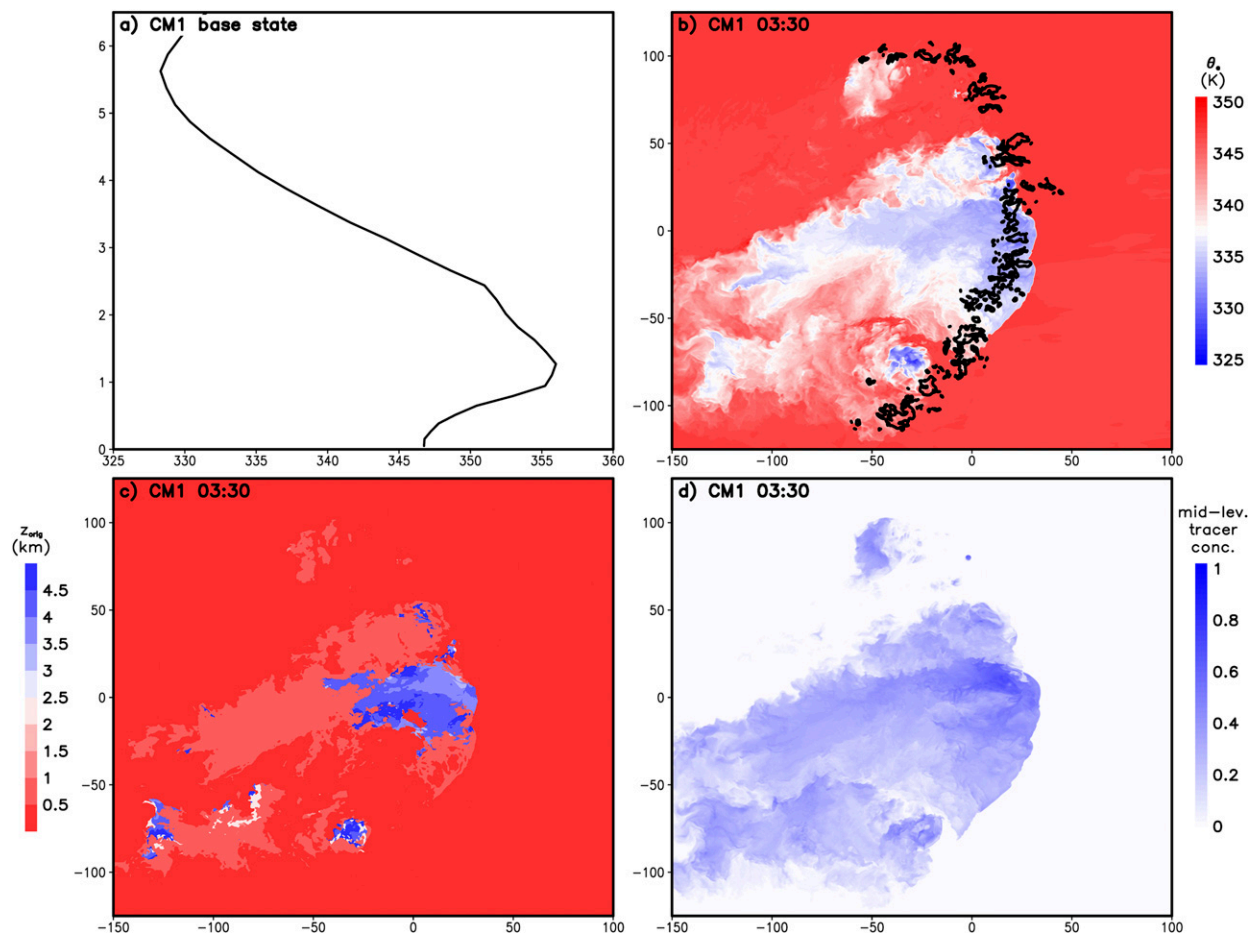


FIG. 13. Depictions of the origins of surface cold pool air at 0330 in the CM1 simulation. (a) Base state vertical profile of equivalent potential temperature ( $\theta_e$ , K). (b) Plan view of surface  $\theta_e$  (shaded in K) and 8 km AGL vertical velocity (contoured in black at  $10 \text{ m s}^{-1}$ ). (c) Origin layer (shaded in km) for the passive tracer with the greatest concentration at each surface grid point. (d) Concentration at the surface of passive tracer that originated from a height  $\geq 3 \text{ km AGL}$ .

rear inflow can be seen impinging upon the system aloft and descending to the surface precisely where the surface cold pool is at its most intense (yellow shading in 11d and 12d).

We finally ask why certain parts of each simulated MCS develop deep surface cold pools and lift copious surface air, while other segments produce little or no surface outflow and appear to remain elevated (examples include the gap at  $y = +50$  to  $+80 \text{ km}$  in Fig. 8b and at  $-95.7^\circ$  to  $-96.3^\circ$  longitude in Fig. 8d). Figure 15 presents both a conservative and a liberal measure of cold pool depth in the CM1 simulation. The depth of the layer with potential temperature ( $\theta$ ) values below that of the ambient environment's surface air (Fig. 15a) is a measure of the minimal upward displacement expected for inflowing air parcels as they ascend along an isentropic surface (assuming an adiabatic process, i.e., that the air is never warmed by condensation). The depth of the layer with

negative buoyancy (represented in Fig. 15b as the layer through which the density potential temperature,  $\theta_\rho$ , is at least 2 K below the ambient pre-MCS air at the same height) includes the surface cold pool as well as the overlying wavelike disturbance (Figs. 9–12), and represents the entire depth of the layer over which inflowing air is expected to receive at least some vertical displacement. In keeping with the previous discussion of the selected cross sections, at its most intense the surface cold pool is at least 1–1.5 km deep (Fig. 15a), which agrees well with the peak depth of 1.7 km computed for the observed case by Hitchcock et al. (2019); the top of the wavelike disturbance is located at 3–4 km AGL (Fig. 15b). Perhaps unsurprisingly, the outflow appears to be deepest where the MCS has been raining the hardest for the longest (swaths of precipitation in Fig. 15c). The parts of the line that remain elevated ( $y = -80$  to  $-70 \text{ km}$

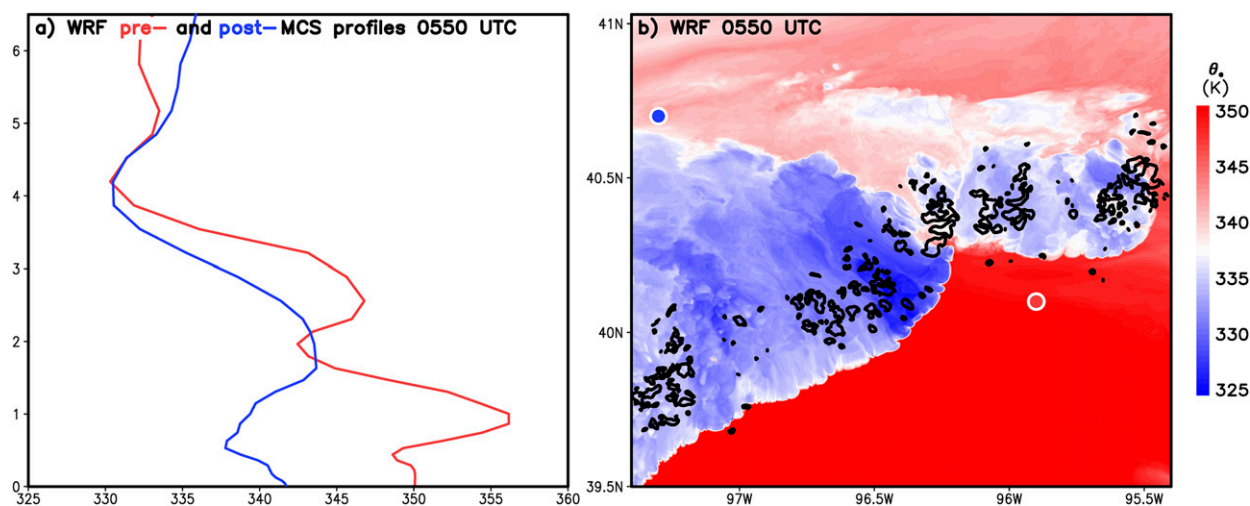


FIG. 14. As in Figs. 13a and 13b, but for the WRF simulation at 0550 UTC. Since the WRF environment is heterogeneous, both pre-MCS (in red) and post-MCS (in blue) profiles of  $\theta_e$  are shown, with the locations of these profiles plotted via filled circles in (b).

and  $y = +50$  to  $+80$  km in Fig. 8b) exhibit little or no surface outflow<sup>4</sup>, and coincide with swaths of minimal prior precipitation in Fig. 15c.

The chaotic details of where pockets of heavier and lighter precipitation will occur are likely not predictable in advance, but it is possible that the MCS retains some memory of these initial pockets via the positive feedback between growth of the cold pool and progressively stronger and deeper lifting of the low-level inflowing air (akin to the “convective memory” described for the tropics by Colin et al. 2019). In short, the self-organizing process is particular to the history of the MCS itself. The same basic evolution also occurs in the WRF simulation (not shown, as computations of cold pool origins and depth become rather convoluted in temporally and spatially varying environments). Notwithstanding its limitations, the CM1 simulation successfully self-organizes a number of the structures seen in the observed MCS, in a way that is not strongly sensitive to the initial convective trigger (animation in Fig. S1). This may suggest that the MCS evolution in this particular case was not overly dependent upon features external to the MCS (e.g., a preexisting stationary front, Figs. 4c,d; a nocturnal low-level jet, Figs. 2 and 4b).

Since the simulated MCSs are at least partly cold pool driven, it is worth considering the degree to which the intensity of the convection might be modulated by

the interplay between the system outflow and the ambient environmental wind shear (i.e., the framework envisioned by Rotunno et al. 1988). The ambient wind profiles depicted in Fig. 2 possess 0–1-km bulk wind shear vectors that point northward, and 0–3-km bulk wind shear vectors that point east-northeastward. Such orientations are primarily parallel to the outflow boundary in this case, which in the Rotunno et al. (1988) framework would correspond to suboptimal lifting (e.g., Coniglio et al. 2012). Instead, it appears that the initial organization and maintenance of convection occurs on the flank of the wavelike disturbance much as shown by Schumacher and Johnson (2008) and Schumacher (2009). In the present case, ascent occurs along the southeastern face of the wave; this is the direction from which the ambient flow produces upglide (the environmental winds are from the east and south between roughly 0.5 and 3.0 km AGL, as shown in Fig. 2). This is quite similar to the importance of the “elevated storm-relative inflow” shown in the case studies of Gale et al. (2002), the simulations of French and Parker (2010), and the climatology of Alfaro and Coniglio (2018). In the WRF simulation there is even stronger preference for redevelopment along the system’s southeastern flank because of the horizontal gradient in instability (Fig. 5), but this self-organizing process is still quite evident along the windward southeastern and eastern faces of the disturbance in the horizontally homogeneous CM1 simulation.

## 5. Production of severe surface winds

During the 0500–0700 UTC period when the observed severe winds emerged (Fig. 1), regional WSR-88Ds revealed the evolution of the MCS toward a severe, cold

<sup>4</sup> The wavelike disturbance (hatched in yellow on Fig. 15b) is still present within the apparent gaps in the cold pool, and looks much as it does in Fig. 9d. But, because the surface air itself does not pass the check for  $\theta_p < -2$  K, the “top of the surface cold pool” is computed as 0 m AGL.

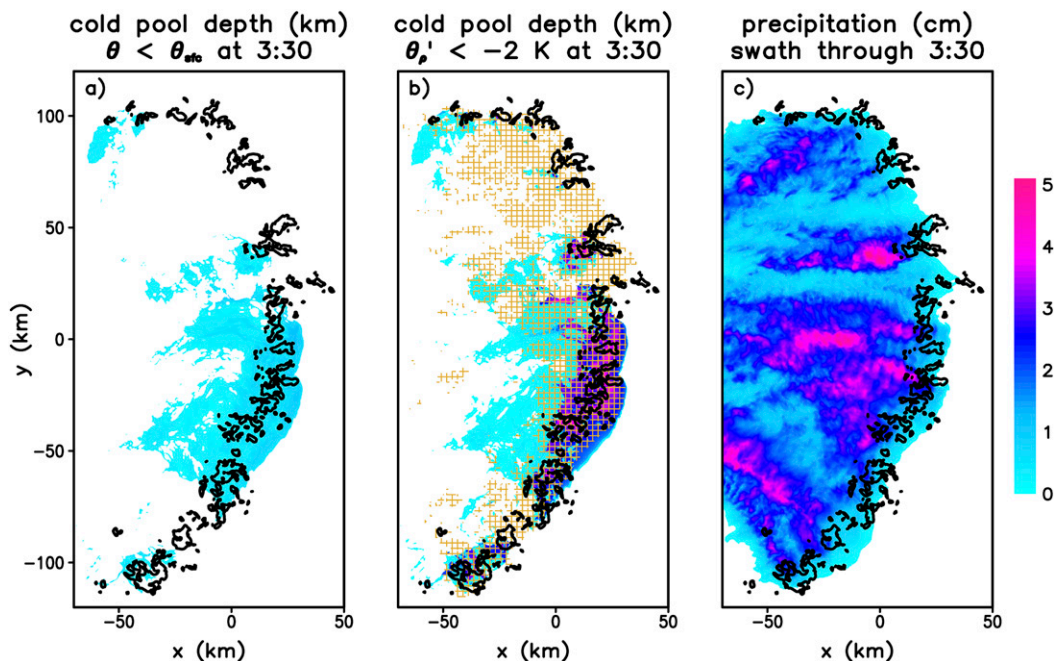


FIG. 15. (a),(b) Two representations of cold pool depth (shaded in km) and (c) accumulated precipitation (shaded in cm) as of 0330 in the CM1 simulation. In (a), the cold pool is represented by the depth of the layer with potential temperature less than the ambient surface value (in other words, this is the height of the surface isentrope). In (b), the cold pool is represented by the depth of the layer with a density potential temperature deficit of 2 K or more (in other words, this is the depth of the layer with locally negative buoyancy). In both cases, it is required that the cold pool condition be met in an uninterrupted layer extending upward from the surface, or else the value is masked. Because this technique removes locations with a wave/bore present aloft but no surface outflow, in (b) the wavelike structures are illustrated by hatching (in yellow) grid points at 2 km AGL with density potential temperature deficit of 2 K or more. Updraft locations are represented by the 8 km AGL vertical velocity (contoured in black at  $10 \text{ m s}^{-1}$ ). The precipitation in (c) is translated by adding on the domain’s motion in 5-min increments, and values less than 1 mm are masked.

pool-driven structure. Rather weak radial convergence was observed at 0508 UTC (Fig. 16a) compared to the distinct gust front with localized radial convergence observed at 0630 UTC (Fig. 16b); this increase in near-ground convergence is further supported in the multi-Doppler wind syntheses of Miller et al. (2019). These two snapshots (Figs. 16a,b) depict internal surges of enhanced velocity (here, inbound radial velocity), both of which are associated with zones of locally maximized cyclonic shear (at base scan altitudes of roughly 600 m AGL). The first severe wind report occurred at 0521 UTC, just southeast of the observed surge position in Fig. 16a. Then, a few minutes before the 0630 UTC base scan observed the surge in Fig. 16b, reports began to occur quite frequently (33 reports<sup>5</sup> within 45 min).

<sup>5</sup> As can be seen in Fig. 1e, of these 33 wind reports 6 were associated with the older bowing segment (near  $-95.5^\circ$  longitude), while 27 were associated with the newly emerging surge farther to the east.

In both cases, embedded bowing segments emerged in the observed radar reflectivity soon after the maxima in cyclonic shear and associated outflow surges developed.

In both the CM1 and WRF simulations, surface winds begin to regularly peak above  $30 \text{ m s}^{-1}$  roughly 3 h after the initiation of convection (e.g., Fig. 7a). Both simulations exhibit internal velocity surges located a small distance behind their respective gust fronts (Figs. 16c,d), and a finescale view reveals that these surges are also associated with centers of cyclonic vorticity (Figs. 16e,f). The horizontal sizes of these surge and cyclonic shear features are similar to the observations although they are slightly more compact (the simulated circulations have diameters of 2.5–4.0 km, as compared to WSR-88D resolved diameters of 3.5–6.0 km; cf. Figs. 16a–d), such that we refer to the simulated structures from here on as “mesovortices”. The importance of embedded mesovortices to severe winds in MCSs is by now well documented (e.g., Atkins et al. 2005; Wakimoto et al. 2006; Wheatley et al. 2006). In all such cases, the simulated velocity surges are

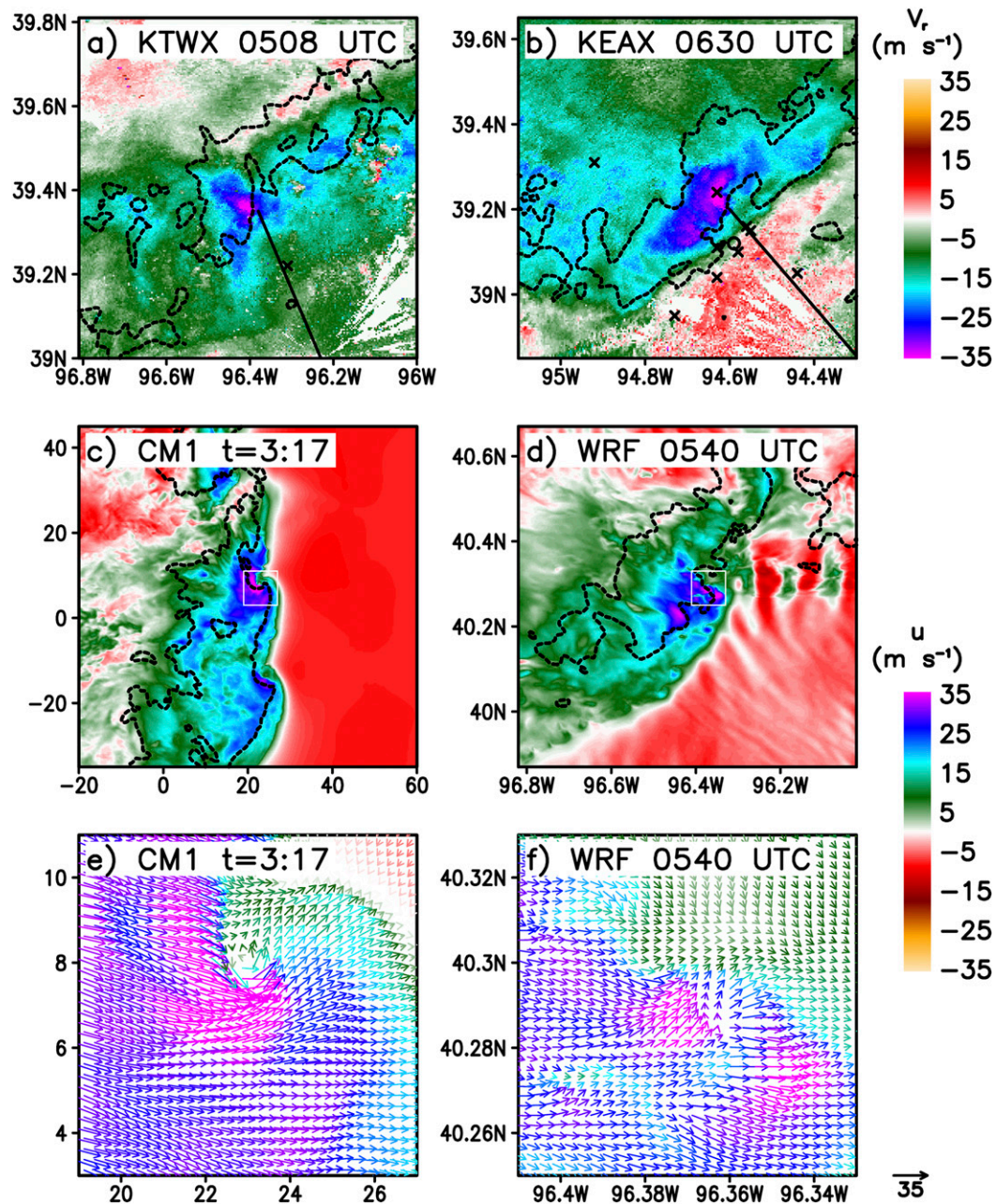


FIG. 16. Radar-observed base scan radial velocity (shaded,  $\text{m s}^{-1}$ ), (a) from Topeka, KS (KTWX), at 0508 UTC, and (b) from Kansas City/Pleasant Hill, MO (KEAX), at 0630 UTC, with a beam shown extending from the radar site to the main vortex/surge (black line). Model simulated 0–500 m AGL maximum ground-relative  $u$  wind (shaded,  $\text{m s}^{-1}$ ) (c) from CM1 model at  $t = 0317$  and (d) from WRF model at 0540 UTC. Model simulated ground-relative horizontal velocity vectors ( $\text{m s}^{-1}$ ) at the bottom model level (e) from CM1 model at  $t = 0317$  and (f) from WRF model at 0540 UTC, with shading reproduced from (c),(d). In (a)–(d), the 45 dBZ value of logarithmic reflectivity factor is dashed in black. Panels (e) and (f) are zoomed depictions of the regions shown by white squares in (c),(d), respectively. The ordering of the color scales is reversed for (c)–(f) [as opposed to (a),(b)] so that the coloring for the strongest winds is mirrored in all panels.

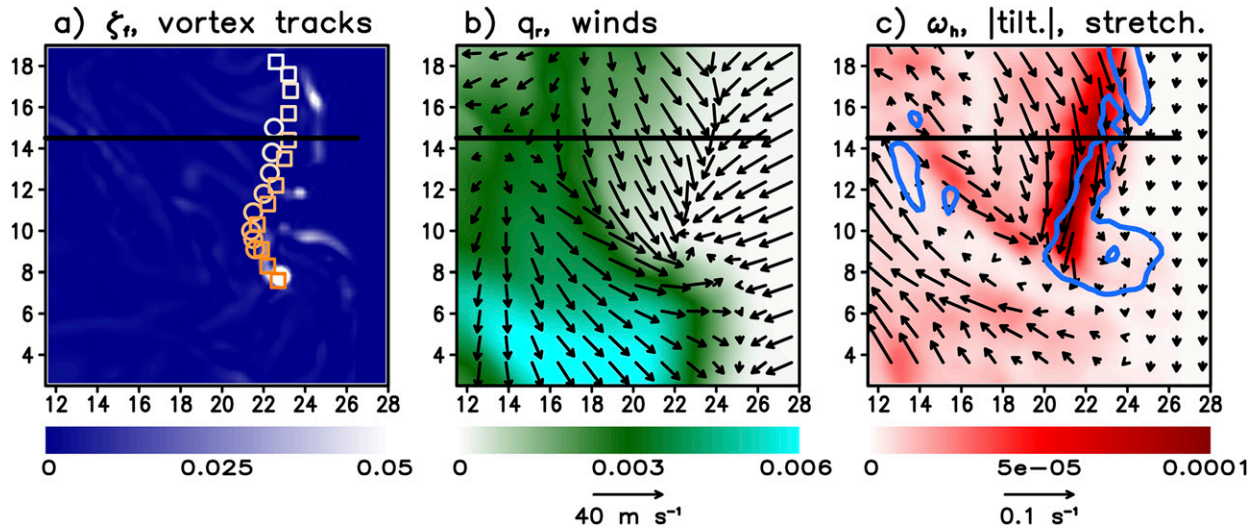


FIG. 17. Depiction of 10-min evolution (from  $t = 0307\text{--}0317$ ) preceding the emergence of the intense surface vortex and severe winds in the CM1 simulation shown in Figs. 16c and 16e. (a) Bottom model level’s final vertical vorticity (shaded,  $s^{-1}$ ) and the positions of two vortices (labeled  $\square$  and  $\circ$ ) are shown at 1-min intervals during the 10-min period. (b) 10-min-averaged rain mixing ratio (shaded,  $kg\ kg^{-1}$ ) and system-relative wind vectors (scaled as shown) at the bottom model level. (c) 10-min-averaged absolute value of tilting of horizontal vorticity (shaded,  $s^{-2}$ ), stretching of vertical vorticity (contoured in blue at  $10^{-5}\ s^{-2}$ ), and horizontal vorticity vectors (scaled as shown) at the bottom model level. The position of the cross section in Fig. 18 is indicated by the heavy black line segments. An animated version of this figure is shown in Fig. S4.

found on the right hand side of the mesovortices (with respect to the system’s motion), as was explained by Wakimoto et al. (2006); the sequential linkage between mesovortex development, outflow surge development, and resultant embedded bowing segments is most easily seen in animations (WRF in Fig. S2 and CM1 in Fig. S3).

In both simulations, as a mesovortex intensifies, the zone of strongest winds becomes quite focused (Figs. 16e,f; Figs. S2 and S3). Given the apparent association between cyclonic shear maxima and the most intense observed and simulated surface winds, we here undertake a physical explanation of the mesovortex origins within both the CM1 and WRF simulations. This is of interest since a rather wide range of possible explanations for MCS mesovortices have been advanced in the literature (e.g., Trapp and Weisman 2003; Wakimoto et al. 2006; Wheatley and Trapp 2008; Atkins and St. Laurent 2009; Schenkman et al. 2012; Xu et al. 2015; Flournoy and Coniglio 2019). The intense vortex from the CM1 simulation that is shown in Fig. 16e originated as a series of individual, weaker vortices that developed behind the system’s gust front, which ultimately began to interact and merge (this is most easily seen in the animation of Fig. S4); such upscale mergers are reminiscent of the MCS mesovortices studied by Flournoy and Coniglio (2019). Two such vortices in the CM1 simulation are marked by the open square ( $\square$ ) and open circle ( $\circ$ ) symbols in Fig. 17a

(and several other pockets of weak cyclonic vorticity can also be seen via the whitest shading). The vortex that is eventually dominant, labeled with  $\square$ , ends with a vertical vorticity of  $0.17\ s^{-1}$  as of  $t = 3:17$  (shown both in Figs. 16e and 17a). Detailed Eulerian and Lagrangian vorticity budgets were computed for the vortices shown in Fig. 17. Unfortunately (as seen in the animated Fig. S4) the large number of vortices, the large horizontal displacements of the vortices between output times, and the overwhelming magnitude of stretching associated with the strongly convergent gust front, made the *origins* of the individual vortices difficult to distill via such budgets. For these reasons, we look at the behavior of the horizontal and vertical vorticity fields in bulk via time averages and vortex lines.

The zone in which both  $\square$  and  $\circ$  (as well as other vortices not shown) emerge is characterized by large, southward-oriented horizontal vorticity (vectors in Fig. 17c). A cross section through this zone (Fig. 18) reveals the existence of a rotor-like circulation just behind the MCS’s gust front (the latter being at  $x^* = 0\ km$  in Fig. 18). Notably, this rotor structure also appears in the observed PECAN multi-Doppler wind syntheses presented for this case by Miller et al. (2019). The simulated pool of southward vorticity ( $\omega_y < 0$ ) is most intense in the lowest 500 m AGL (Fig. 18), and is consistent with the expected baroclinic generation of horizontal vorticity near an outflow boundary (e.g., Rotunno et al. 1988). In the CM1 simulation at

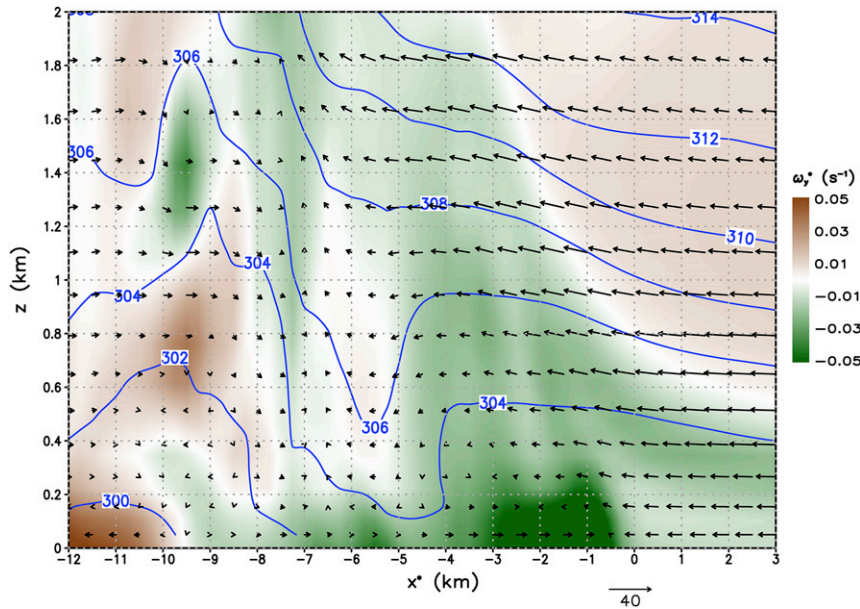


FIG. 18. Vertical cross section depicting averages of horizontal vorticity about an axis normal to the cross section ( $\text{s}^{-1}$ , shaded), density potential temperature (K, contoured in blue), and wind vectors ( $\text{m s}^{-1}$ , scaled as shown) tangent to the cross section, for the CM1 simulation at  $t = 0308$  (this is 9 min prior to Fig. 16e, when the vortices tracked in Fig. 17 have first become evident in surface vertical vorticity). Green shading corresponds to horizontal vorticity oriented out of the page (brown shading: into the page). All axis labels are in km (the  $x^*$  coordinate is relative to the outflow boundary), and the position of the cross section is shown by the solid black line segment in Fig. 17. The averages are taken within a 5-km-wide horizontal swath that is centered on the black line segment (i.e., 2.5 km on either side normal to the vertical cross section).

this location and time, the virtual potential temperature gradient is still rather weak, but the gradient in precipitation mixing ratio (Fig. 17b) is sufficient to support a modest eastward-pointing gradient in buoyancy (as visualized by density potential temperature contours in Fig. 18). Where both  $\square$  and  $\circ$  develop there is production of vertical vorticity of both signs as the large horizontal vorticity of the rotor is superposed with gradients in vertical velocity associated with gust front updrafts (Fig. 17c shows the time-averaged magnitude of the tilting rate because the changing positions of updrafts cause substantial cancellation between positive and negative tilting maxima at individual grid points over the 10-min window). The vortices ( $\square$  and  $\circ$ ) then amplify via convergence (blue contour in Fig. 17c) as they travel southward.

Multiple vortices form from these small-scale tilting events and move southward largely independently (animation in Fig. S4). The ultimate peak in cyclonic vertical vorticity and subsequent velocity surge then occur when an intense core of rain and graupel begins to fall out to their south (visible at  $y = 6$  km in Fig. 17b). This heavy precipitation produces a zone of convergence on its northern side; as a result, the southward-moving

vortices slow down there and begin to merge (this is revealed by the bullseye in the convergence forcing term contoured in blue in Fig. 17c). The 3D linkages between the rotor and the developing vortices become quite clear through the visualization of vortex lines (Fig. 19). All of the vortex lines in the vicinity point southward (in keeping with the vorticity vectors shown in Fig. 17c). The two featured cyclonic vortices ( $\square$  and  $\circ$ ) are linked to locations where the southward-pointing vortex lines have been displaced to the ground, embodying the basic vortex–genesis mechanism first proposed by Trapp and Weisman (2003).

The vortices in the WRF simulation are a bit less distinctive looking (Fig. 16f), and have lower peak values of vertical vorticity (just over  $0.05 \text{ s}^{-1}$ ) than those in CM1, perhaps due to small environmental differences in the heterogeneous WRF, but also presumably because of the coarser model grid spacing, the inclusion of parameterized boundary layer mixing, and possibly the inclusion of surface drag. As in CM1, multiple vortices form and interact with one another (annotated in Fig. 20a, animated in Fig. S5), with the vortices emerging from a zone where the magnitude

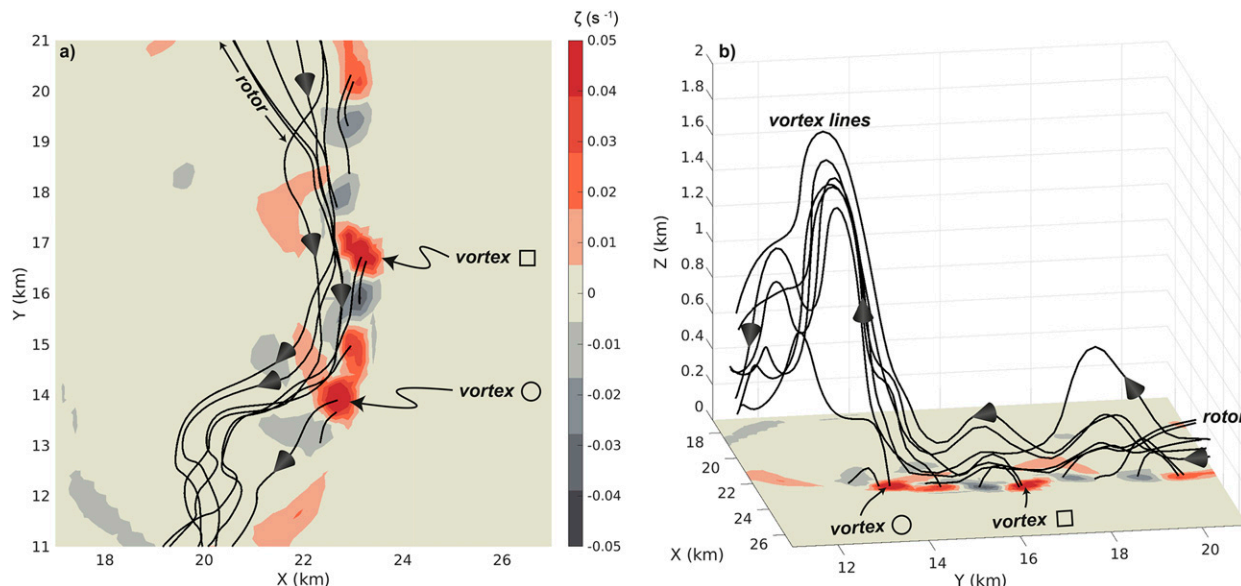


FIG. 19. (a) Plan view and (b) 3D rendering of vertical vorticity at the bottom model level (shaded,  $s^{-1}$ ) and vortex lines (plotted in black) for the CM1 simulation at  $t = 0308$  (this is 9 min prior to Fig. 16e, when the vortices tracked in Fig. 17 have first become evident in surface vertical vorticity). Orientation of the vortex lines is indicated by the black arrowhead annotations. Cyclonic vortices that appear in Fig. 17 are labeled with the same symbols for reference.

of the tilting term<sup>6</sup> is persistently large (shading in Fig. 20c), and then amplifying within a zone of convergence (Fig. 20b) and vorticity stretching (blue contours in Fig. 20c). However, in the WRF realization, the vortices form a bit farther behind the main gust front than in CM1, and their motion is more nearly perpendicular to the gust front. This suggests the possibility of a formation mechanism that is distinct from the one identified in the CM1 simulation.

At the time and location of the analyzed vortex formation, the WRF simulation has a substantially stronger cold pool than the CM1 simulation (cf. density potential temperature contours in Fig. 18 vs Fig. 21). This may partly be due to the spatially varying environment in the WRF simulation, but also is likely influenced by the different microphysical parameterizations used in the two simulations. Notwithstanding their different cold pool strengths, the most significant difference in the overall structure of the WRF simulation is that the low-level horizontal vorticity vectors point northeastward (Fig. 20c), almost directly opposite of those in the CM1 simulation (and opposite of what one would expect from baroclinic generation). Cross sections show that this northeastward-pointing horizontal vorticity extends up to a height of roughly 200 m, and

is clearly associated with a frictional deceleration of the northwesterly outflow winds below that level (Fig. 21). Frictional generation of horizontal vorticity has been previously implicated in the genesis of MCS mesovortices by Schenkman et al. (2012) and Xu et al. (2015).

Predictably, the vortex lines become more complicated in the WRF simulation, with Coriolis, surface drag, and a boundary layer parameterization included. Notwithstanding these caveats, five well-behaved vortex lines attached to centers of surface vorticity in the WRF simulation provide at least a partial picture of the likely associated processes (Fig. 22). Two of the vortices, labeled  $\square$  and  $\circ$ , are attached to vortex lines (colored blue in Fig. 22) that turn southwestward in the 1–3 km AGL layer, which would be consistent with a baroclinically associated source of horizontal vorticity (the negative values in Fig. 21). Two of the vortices, labeled with a triangle ( $\triangle$ ) and “anticyclonic vortex”, are attached to vortex lines (colored red in Fig. 22) that turn northeastward in the 0–400 m AGL layer, which would be consistent with a frictionally associated source of horizontal vorticity (the positive values in Fig. 21). A fifth vortex, labeled with a diamond ( $\diamond$ ), is attached to a “hybrid” vortex line (colored black in Fig. 22) that turns northeastward in the lowest 300 m AGL (presumably friction-associated) but then turns back southwestward above 700 m AGL (presumably baroclinity-associated). In short, it seems possible that both

<sup>6</sup>The WRF vortex–genesis data are presented in the same way as the CM1 data, for the same reasons mentioned previously.

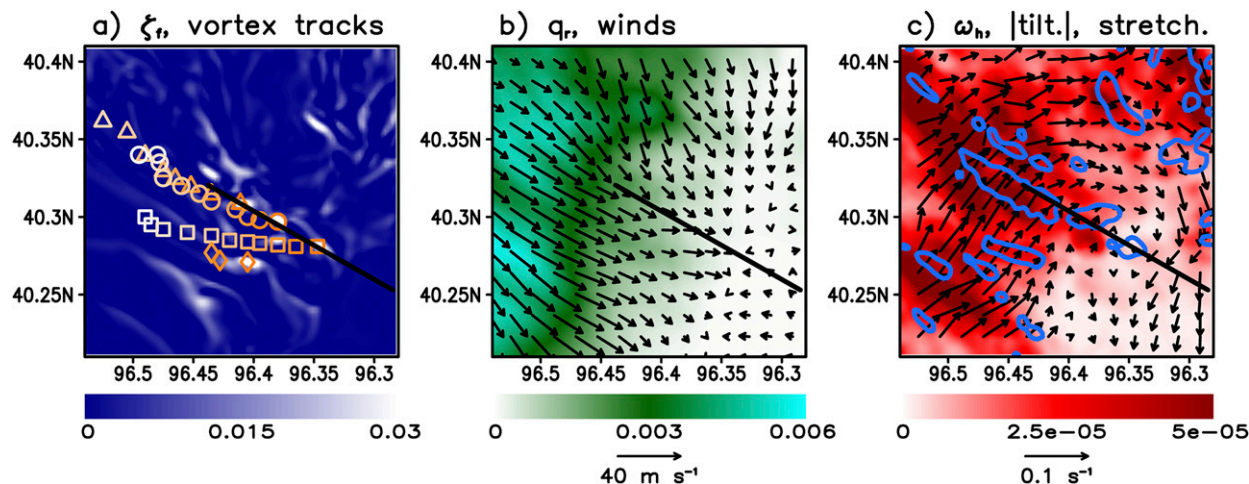


FIG. 20. As in Fig. 17, but for the WRF simulation during the time period 0530–0540 UTC. Note that the shading scales in (a), (c) differ from Fig. 17. In (a) the positions of four vortices (labeled  $\square$ ,  $\circ$ ,  $\triangle$ , and  $\diamond$ ) are at 1-min intervals during the 10-min period. The position of the cross section in Fig. 21 is indicated by the heavy black line segments. An animated version of this figure is shown in Fig. S5.

frictionally generated and baroclinically generated horizontal vorticity are serving (via tilting) as sources for surface vortices in this simulation.

The attribute common to both simulations is that the sources of horizontal vorticity that are subsequently tilted originate in the MCSs' outflow sectors, as no vortex lines were found in either simulation that connected to the ambient pre-gust front environment (many more were examined but not shown). Such a finding is distinct from the more inflow-centered mesovortex mechanism described in mature MCSs by Atkins and

St. Laurent (2009) (and at least partially contributing in the study by Flournoy and Coniglio 2019); this is perhaps surprising considering the large influx of ambient streamwise vorticity found in the inflow environment (storm-relative helicity of  $646 \text{ m}^2 \text{ s}^{-2}$  observed,  $757 \text{ m}^2 \text{ s}^{-2}$  in the WRF sounding). Instead, a model configured in the traditional, idealized way (the CM1 simulation) seems to produce mesovortices via the Trapp and Weisman (2003) outflow pathway. The more “process-inclusive” model configuration (the WRF simulation) has similarities to the Trapp and Weisman (2003)

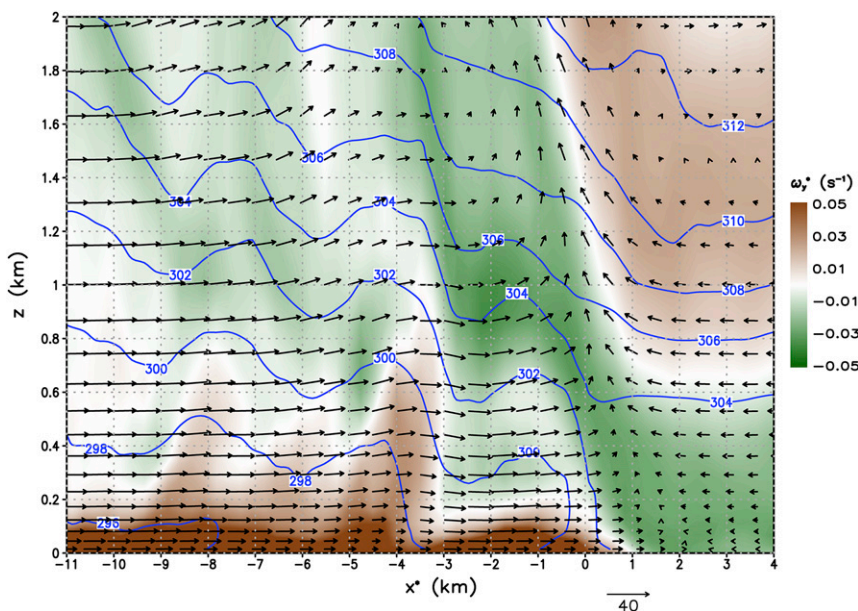


FIG. 21. As in Fig. 18, but for the WRF simulation at 0540 UTC. The position of the cross section is shown by the solid black line segment in Fig. 20.

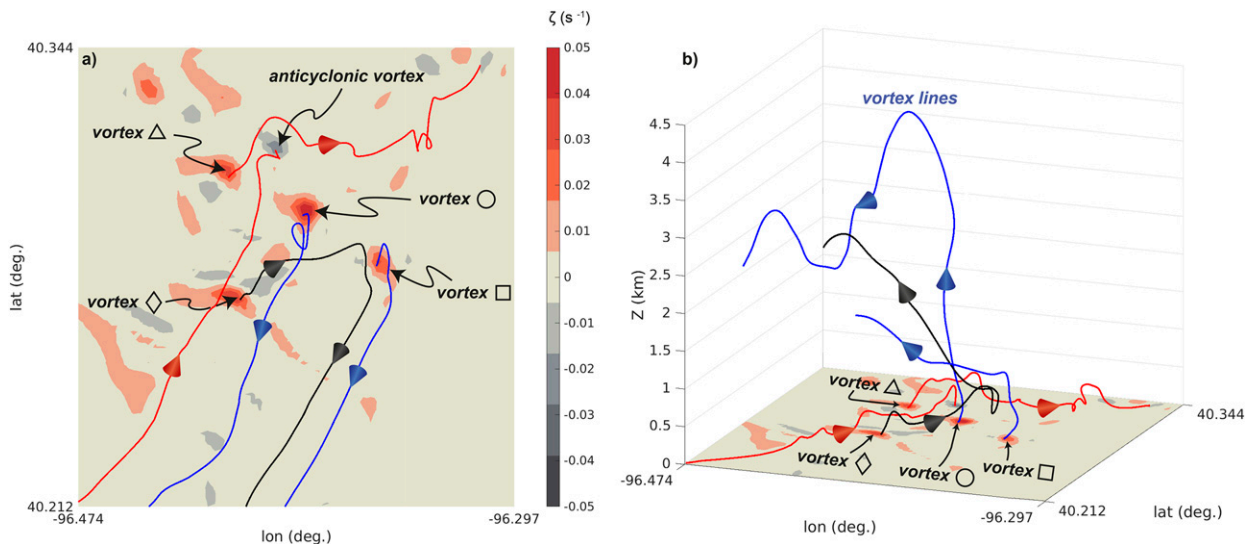


FIG. 22. As in Fig. 19, but for 0540 UTC in the WRF simulation. Vortex lines with orientations and altitudes that are consistent with frictional horizontal vorticity are colored red. Vortex lines with orientations and altitudes that are consistent with baroclinic horizontal vorticity are colored blue. A hybrid vortex line is colored black. Cyclonic vortices that appear in Fig. 20 are labeled with the same symbols for reference; an anticyclonic vortex (mentioned in the text) is also labeled for reference.

conceptual model, but it appears that surface drag may be a major source of horizontal vorticity that can eventually be tilted, as also concluded by Schenkman et al. (2012) and Xu et al. (2015). In both models, the vortex genesis process precedes the development of the most intense wind surges and embedded bow echo structures.

### 6. Conclusions

The 25–26 June 2015 PECAN MCS was initiated around local sunset (just before 0300 UTC) and developed into a classical convective line with trailing stratiform precipitation and severe surface winds in eastern Kansas and western Missouri. This case provided an excellent opportunity to investigate the mechanisms associated with nocturnal MCS evolution, structure, and severity. To supplement a study based solely on the PECAN field observations from earlier in the MCS’s life (Miller et al. 2019), we used a pair of numerical simulations with differing levels of complexity. A highly idealized CM1 simulation was used to isolate the self-generated aspects of the MCS, which served as a means for comparison to the more process-inclusive WRF case study simulation.

#### a. Primary findings

Based upon conventional parameters (CAPE, CIN, height of the LFC, etc.) the 25–26 June MCS environment would be conventionally thought to support elevated convection, having substantial near-ground

stability and its most unstable parcels at or above 1 km AGL. Initially the simulated convective systems were indeed elevated, and lacked appreciable surface cold pools. Rather, they were maintained by wavelike disturbances, which developed in response to initial convective heating aloft and produced subsequent ascent on their windward faces (as also seen in the elevated MCSs studied by Schumacher and Johnson 2008; Schumacher 2009). As the simulated systems matured, pockets of cold surface outflow began to appear, particularly where the heaviest precipitation occurred. The particular history of an MCS’s precipitation pattern is thus relevant to its subsequent self-organization by outflows. Based upon its equivalent potential temperature, the air in the surface cold pools appears to have originated from up to 4–5 km AGL. Depending upon how one defines their tops, these cold pools eventually became 1.5–3.5 km deep. Based upon the PECAN soundings analyzed by Hitchcock et al. (2019), it appears that such cold pools are rather common in nocturnal MCSs. Soon after surface cold pools were established, passive tracers suggest that the simulated convection was no longer decoupled from the near-surface layer. Much as in the observed “elevated initiation” MCS studied by Marsham et al. (2011), the message of these simulations is that nocturnal convective initiation can still lead to cold pool–driven, surface-based MCSs.

Soon after this transition, severe surface winds ensued in both simulations. In both the observations and the models, the strongest of these winds appear to have

been affiliated with embedded low-level centers of vorticity and their attendant outflow surges (which in turn led to internal bow echo structures). In both model realizations, downward tilting of horizontal vorticity that is present within the outflow seems to be a likely source of the near-ground rotation. The origins of this outflow horizontal vorticity within the highly idealized CM1 framework appear to be baroclinic, such that the vortex–genesis pathway bears great resemblance to the pioneering study of [Trapp and Weisman \(2003\)](#). The origins of outflow horizontal vorticity in the less-idealized WRF framework appear to be more complicated, and quite likely involve surface friction, as in the studies of [Schenkman et al. \(2012\)](#) and [Xu et al. \(2015\)](#). In either case, the evolution toward cold pool–driven, surface-based convection in this nocturnal MCS seems to be a precursor for severe wind production via mechanisms that are quite reminiscent of daytime MCSs. Although severe surface winds are certainly not impossible in convective storms that remain elevated (e.g., the climatology of [Horgan et al. 2007](#), and the case studies cited in [section 1](#)), there is mounting evidence that many nocturnal and post-frontal MCSs end up bearing strong resemblance to classical severe MCSs occurring in afternoon, warm sector conditions.

#### *b. Future work*

Much of what has been learned about MCS dynamics to date has emerged from idealized simulations like the one embodied here by the CM1 model. While the CM1 results suggest that many of the studied MCS structures are self-generated, the community must grapple with the comparative importance of the omitted processes in idealized runs. For example, the inclusion in the WRF simulation of a temporally and spatially varying environment appears to add realism, but also hinders the controlled isolation of individual mechanisms. Along these lines, it is interesting that CM1 simulations initialized with the observed PECAN soundings failed to produce long-lived MCSs, necessitating the ultimate use of a point sounding from the WRF simulation. It seems likely that, although the simulated CM1 MCS was self-organizing, it still indirectly relied on preconditioning of the environment by synoptic and/or mesoscale processes, as were represented in the WRF simulation. It would be worthwhile to know the extent to which nocturnal MCSs directly owe their maintenance and evolution to features such as middle tropospheric waves, surface fronts, and low-level jets. The present case was rather weakly forced, so perhaps the impacts of the larger scales would be greater in other (e.g., cold frontal) cases. As a first

step toward addressing this question, we are preparing a more longitudinal study comparing four of the most intense and well-observed MCSs from PECAN in the idealized versus real-world frameworks.

The omission of surface and boundary layer processes from idealized models may be equally consequential; in particular, the inclusion of surface drag in the WRF simulation here added horizontal vorticity to the storm outflow that was opposite in sign and greater in magnitude than the commonly discussed, baroclinically generated vorticity. In addition to the implications for mesovortex generation, one might even ask how the benchmark theory of [Rotunno et al. \(1988, i.e., an optimal balance between baroclinically produced horizontal vorticity in the cold pool and environmental shear\)](#) ought to be applied when surface drag is a major, opposite-signed source of horizontal vorticity in the cold pool. In general, more work is needed on the representation of surface drag and boundary layer mixing in studies of storm dynamics (e.g., [Markowski and Bryan 2016](#); [Markowski 2018](#)); the associated uncertainties in numerical models are likely even greater in nocturnal stable boundary layers (e.g., [Holtzlag et al. 2013](#)), such as were observed during PECAN.

Finally, it would be of societal benefit to connect the principal elements revealed in this study (development of surface cold pools, self-organization, transition to surface-based convection, generation of mesovortices) to the pressing operational problem of nocturnal severe wind forecasting. To do so, a richer understanding of the spectrum of environmental responses to convection (cold pools, gravity waves, and bores) will likely be needed, in addition to a careful examination of worthwhile environmental proxies for them. The PECAN campaign yielded a large number of useful nocturnal datasets to support such research.

*Acknowledgments.* George Bryan is gratefully acknowledged for providing and supporting the CM1 model. Simulations were accomplished with high-performance computing support from Yellowstone ([ark:/85065/d7wd3xhc](#)) and Cheyenne ([doi:10.5065/D6RX99HX](#)) provided by NCAR's Computational and Information Systems Laboratory, sponsored by the National Science Foundation. This work was supported by the National Science Foundation under Grants AGS-1359709 and AGS-1359726. The authors thank the members of the NCSU Convective Storms Group for their beneficial comments, and the many field workers from the PECAN campaign for their late night travail in acquiring the observational data. Dr. Michael Coniglio, Dr. Kevin Haghi, and two anonymous reviewers also

provided many helpful suggestions during the review process.

## REFERENCES

- Alfaro, D. A., and M. C. Coniglio, 2018: Discrimination of mature and dissipating severe-wind-producing MCSs with layer-lifting indices. *Wea. Forecasting*, **33**, 3–21, <https://doi.org/10.1175/WAF-D-17-0088.1>.
- Atkins, N. T., and M. St. Laurent, 2009: Bow echo mesovortices. Part II: Their genesis. *Mon. Wea. Rev.*, **137**, 1514–1532, <https://doi.org/10.1175/2008MWR2650.1>.
- , C. S. Bouchard, R. W. Przybylinski, R. J. Trapp, and G. Schmocker, 2005: Damaging surface wind mechanisms within the 10 June 2003 Saint Louis bow echo during BAMEX. *Mon. Wea. Rev.*, **133**, 2275–2296, <https://doi.org/10.1175/MWR2973.1>.
- Augustine, J. A., and F. Caracena, 1994: Lower-tropospheric precursors to nocturnal MCS development over the central United States. *Wea. Forecasting*, **9**, 116–135, [https://doi.org/10.1175/1520-0434\(1994\)009<0116:LTPTNM>2.0.CO;2](https://doi.org/10.1175/1520-0434(1994)009<0116:LTPTNM>2.0.CO;2).
- Bernardet, L. R., and W. R. Cotton, 1998: Multiscale evolution of a derecho-producing mesoscale convective system. *Mon. Wea. Rev.*, **126**, 2991–3015, [https://doi.org/10.1175/1520-0493\(1998\)126<2991:MEOADP>2.0.CO;2](https://doi.org/10.1175/1520-0493(1998)126<2991:MEOADP>2.0.CO;2).
- Billings, J. M., and M. D. Parker, 2012: Evolution and maintenance of the 22–23 June 2003 nocturnal convection during BAMEX. *Wea. Forecasting*, **27**, 279–300, <https://doi.org/10.1175/WAF-D-11-00056.1>.
- Blake, B. T., D. B. Parsons, K. R. Haghi, and S. G. Castleberry, 2017: The structure, evolution, and dynamics of a nocturnal convective system simulated using the WRF-ARW model. *Mon. Wea. Rev.*, **145**, 3179–3201, <https://doi.org/10.1175/MWR-D-16-0360.1>.
- Bosart, L. F., and A. Seimon, 1988: A case study of an unusually intense atmospheric gravity wave. *Mon. Wea. Rev.*, **116**, 1857–1886, [https://doi.org/10.1175/1520-0493\(1988\)116<1857:ACSOAU>2.0.CO;2](https://doi.org/10.1175/1520-0493(1988)116<1857:ACSOAU>2.0.CO;2).
- Browning, K., J. Marsham, J. Nicol, F. Perry, B. White, A. Blyth, and S. Mobbs, 2010: Observations of dual slantwise circulations above a cool undercurrent in a mesoscale convective system. *Quart. J. Roy. Meteor. Soc.*, **136**, 354–373, <https://doi.org/10.1002/qj.582>.
- Bryan, G. H., and J. M. Fritsch, 2002: A benchmark simulation for moist nonhydrostatic numerical models. *Mon. Wea. Rev.*, **130**, 2917–2928, [https://doi.org/10.1175/1520-0493\(2002\)130<2917:ABSFMN>2.0.CO;2](https://doi.org/10.1175/1520-0493(2002)130<2917:ABSFMN>2.0.CO;2).
- , and M. D. Parker, 2010: Observations of a squall line and its near environment using high-frequency rawinsonde launches during VORTEX2. *Mon. Wea. Rev.*, **138**, 4076–4097, <https://doi.org/10.1175/2010MWR3359.1>.
- , and H. Morrison, 2012: Sensitivity of a simulated squall line to horizontal resolution and parameterization of microphysics. *Mon. Wea. Rev.*, **140**, 202–225, <https://doi.org/10.1175/MWR-D-11-00046.1>.
- Buzzi, A., M. Fantini, and G. Lippolis, 1991: Quasi-stationary organized convection in the presence of an inversion near the surface: Experiments with a 2-D numerical model. *Meteor. Atmos. Phys.*, **45**, 75–86, <https://doi.org/10.1007/BF01027476>.
- Carbone, R. E., J. D. Tuttle, D. A. Ahijevych, and S. B. Trier, 2002: Inferences of predictability associated with warm season precipitation episodes. *J. Atmos. Sci.*, **59**, 2033–2056, [https://doi.org/10.1175/1520-0469\(2002\)059<2033:IOPAWW>2.0.CO;2](https://doi.org/10.1175/1520-0469(2002)059<2033:IOPAWW>2.0.CO;2).
- Chen, F., and J. Dudhia, 2001: Coupling an advanced land surface–hydrology model with the Penn State–NCAR MM5 modeling system. Part I: Model implementation and sensitivity. *Mon. Wea. Rev.*, **129**, 569–585, [https://doi.org/10.1175/1520-0493\(2001\)129<0569:CAALSH>2.0.CO;2](https://doi.org/10.1175/1520-0493(2001)129<0569:CAALSH>2.0.CO;2).
- Colin, M., S. Sherwood, O. Geoffroy, S. Bony, and D. Fuchs, 2019: Identifying the sources of convective memory in cloud-resolving simulations. *J. Atmos. Sci.*, **76**, 947–962, <https://doi.org/10.1175/JAS-D-18-0036.1>.
- Colman, B. R., 1990: Thunderstorms above frontal surfaces in environments without positive CAPE. Part I: A climatology. *Mon. Wea. Rev.*, **118**, 1103–1121, [https://doi.org/10.1175/1520-0493\(1990\)118<1103:TAFSIE>2.0.CO;2](https://doi.org/10.1175/1520-0493(1990)118<1103:TAFSIE>2.0.CO;2).
- Coniglio, M. C., S. F. Corfidi, and J. S. Kain, 2012: Views on applying RKW theory: An illustration using the 8 May 2009 derecho-producing convective system. *Mon. Wea. Rev.*, **140**, 1023–1043, <https://doi.org/10.1175/MWR-D-11-00026.1>.
- Corfidi, S. F., S. J. Corfidi, and D. M. Schultz, 2008: Elevated convection and castellanus: Ambiguities, significance, and questions. *Wea. Forecasting*, **23**, 1280–1303, <https://doi.org/10.1175/2008WAF222118.1>.
- Crook, N. A., and M. W. Moncrieff, 1988: The effect of large-scale convergence on the generation and maintenance of deep moist convection. *J. Atmos. Sci.*, **45**, 3606–3624, [https://doi.org/10.1175/1520-0469\(1988\)045<3606:TEOLSC>2.0.CO;2](https://doi.org/10.1175/1520-0469(1988)045<3606:TEOLSC>2.0.CO;2).
- Davis, C. A., K. W. Manning, R. E. Carbone, S. B. Trier, and J. D. Tuttle, 2003: Coherence of warm-season continental rainfall in numerical weather prediction models. *Mon. Wea. Rev.*, **131**, 2667–2679, [https://doi.org/10.1175/1520-0493\(2003\)131<2667:COWCRI>2.0.CO;2](https://doi.org/10.1175/1520-0493(2003)131<2667:COWCRI>2.0.CO;2).
- Deardorff, J. W., 1980: Stratocumulus-capped mixed layers derived from a three-dimensional model. *Bound.-Layer Meteor.*, **18**, 495–527, <https://doi.org/10.1007/BF00119502>.
- Dudhia, J., 1989: Numerical study of convection observed during the Winter Monsoon Experiment using a mesoscale two-dimensional model. *J. Atmos. Sci.*, **46**, 3077–3107, [https://doi.org/10.1175/1520-0469\(1989\)046<3077:NSOCOD>2.0.CO;2](https://doi.org/10.1175/1520-0469(1989)046<3077:NSOCOD>2.0.CO;2).
- , M. W. Moncrieff, and D. W. K. So, 1987: The two-dimensional dynamics of West African squall lines. *Quart. J. Roy. Meteor. Soc.*, **113**, 121–146, <https://doi.org/10.1002/qj.49711347508>.
- Flournoy, M. D., and M. C. Coniglio, 2019: Origins of vorticity in a simulated tornadic mesovortex observed during PECAN on 6 July 2015. *Mon. Wea. Rev.*, **147**, 107–134, <https://doi.org/10.1175/MWR-D-18-0221.1>.
- Fovell, R. G., G. L. Mullendore, and S.-H. Kim, 2006: Discrete propagation in numerically simulated nocturnal squall lines. *Mon. Wea. Rev.*, **134**, 3735–3752, <https://doi.org/10.1175/MWR3268.1>.
- French, A. J., and M. D. Parker, 2010: The response of simulated nocturnal convective systems to a developing low-level jet. *J. Atmos. Sci.*, **67**, 3384–3408, <https://doi.org/10.1175/2010JAS3329.1>.
- Fritsch, J. M., and G. S. Forbes, 2001: Mesoscale convective systems. *Severe Convective Storms, Meteor. Monogr.*, No. 50, Amer. Meteor. Soc., 323–357.
- , and R. E. Carbone, 2004: Improving quantitative precipitation forecasts in the warm season. *Bull. Amer. Meteor. Soc.*, **85**, 955–965, <https://doi.org/10.1175/BAMS-85-7-955>.
- , R. J. Kane, and C. R. Chelius, 1986: The contribution of mesoscale convective weather systems to the warm-season precipitation in the United States. *J. Climate Appl. Meteor.*, **25**,

- 1333–1345, [https://doi.org/10.1175/1520-0450\(1986\)025<1333:TCOMCW>2.0.CO;2](https://doi.org/10.1175/1520-0450(1986)025<1333:TCOMCW>2.0.CO;2).
- Gale, J. J., W. A. Gallus, and K. A. Jungbluth, 2002: Toward improved prediction of mesoscale convective system dissipation. *Wea. Forecasting*, **17**, 856–872, [https://doi.org/10.1175/1520-0434\(2002\)017<0856:TIPOMC>2.0.CO;2](https://doi.org/10.1175/1520-0434(2002)017<0856:TIPOMC>2.0.CO;2).
- Geerts, B., and Coauthors, 2017: The 2015 Plains Elevated Convection At Night field project. *Bull. Amer. Meteor. Soc.*, **98**, 767–786, <https://doi.org/10.1175/BAMS-D-15-00257.1>.
- Haertel, P. T., R. H. Johnson, and S. N. Tulich, 2001: Some simple simulations of thunderstorm outflows. *J. Atmos. Sci.*, **58**, 504–516, [https://doi.org/10.1175/1520-0469\(2001\)058<0504:SSSOTO>2.0.CO;2](https://doi.org/10.1175/1520-0469(2001)058<0504:SSSOTO>2.0.CO;2).
- Hitchcock, S. M., R. S. Schumacher, G. R. Herman, M. C. Coniglio, M. D. Parker, and C. L. Ziegler, 2019: Evolution of pre- and postconvective environmental profiles from mesoscale convective systems during PECAN. *Mon. Wea. Rev.*, **147**, 2329–2354, <https://doi.org/10.1175/MWR-D-18-0231.1>.
- Holtzlag, A. A. M., and Coauthors, 2013: Stable atmospheric boundary layers and diurnal cycles: Challenges for weather and climate models. *Bull. Amer. Meteor. Soc.*, **94**, 1691–1706, <https://doi.org/10.1175/BAMS-D-11-00187.1>.
- Horgan, K. L., D. M. Schultz, J. E. Hales, S. F. Corfidi, and R. H. Johns, 2007: A five-year climatology of elevated severe convective storms in the United States east of the Rocky Mountains. *Wea. Forecasting*, **22**, 1031–1044, <https://doi.org/10.1175/WAF1032.1>.
- Janjić, Z. I., 2002: Nonsingular implementation of the Mellor–Yamada level 2.5 scheme in the NCEP Meso model. NCEP Office Note 437, 61 pp.
- Johns, R. H., and W. D. Hirt, 1987: Derechos: Widespread convectively induced windstorms. *Wea. Forecasting*, **2**, 32–49, [https://doi.org/10.1175/1520-0434\(1987\)002<0032:DWCIW>2.0.CO;2](https://doi.org/10.1175/1520-0434(1987)002<0032:DWCIW>2.0.CO;2).
- Kain, J. S., 2004: The Kain–Fritsch convective parameterization: An update. *J. Appl. Meteor.*, **43**, 170–181, [https://doi.org/10.1175/1520-0450\(2004\)043<0170:TKCPAU>2.0.CO;2](https://doi.org/10.1175/1520-0450(2004)043<0170:TKCPAU>2.0.CO;2).
- , and J. M. Fritsch, 1993: Convective parameterization for mesoscale models: The Kain–Fritsch scheme. *The Representation of Cumulus Convection in Numerical Models, Meteor. Monogr.*, No. 46, Amer. Meteor. Soc., 165–170.
- Klemp, J. B., W. C. Skamarock, and J. Dudhia, 2007: Conservative split-explicit time integration methods for the compressible nonhydrostatic equations. *Mon. Wea. Rev.*, **135**, 2897–2913, <https://doi.org/10.1175/MWR3440.1>.
- Knupp, K. R., 1996: Structure and evolution of a long-lived, microburst-producing storm. *Mon. Wea. Rev.*, **124**, 2785–2806, [https://doi.org/10.1175/1520-0493\(1996\)124<2785:SAEOAL>2.0.CO;2](https://doi.org/10.1175/1520-0493(1996)124<2785:SAEOAL>2.0.CO;2).
- Laing, A. G., and J. M. Fritsch, 2000: The large-scale environments of the global populations of mesoscale convective complexes. *Mon. Wea. Rev.*, **128**, 2756–2776, [https://doi.org/10.1175/1520-0493\(2000\)128<2756:TLSEOT>2.0.CO;2](https://doi.org/10.1175/1520-0493(2000)128<2756:TLSEOT>2.0.CO;2).
- MacIntosh, C. W., and M. D. Parker, 2017: The 6 May 2010 elevated supercell during VORTEX2. *Mon. Wea. Rev.*, **145**, 2635–2657, <https://doi.org/10.1175/MWR-D-16-0329.1>.
- Maddox, R. A., 1980: Mesoscale convective complexes. *Bull. Amer. Meteor. Soc.*, **61**, 1374–1387, [https://doi.org/10.1175/1520-0477\(1980\)061<1374:MCC>2.0.CO;2](https://doi.org/10.1175/1520-0477(1980)061<1374:MCC>2.0.CO;2).
- Markowski, P. M., 2018: A review of the various treatments of the surface momentum flux in severe storms simulations: Assumptions, deficiencies, and alternatives. *29th Conf. on Severe Local Storms*, Stowe, VT, Amer. Meteor. Soc., 7.3, <https://ams.confex.com/ams/29SLS/webprogram/Paper348116.html>.
- , and G. H. Bryan, 2016: LES of laminar flow in the PBL: A potential problem for convective storm simulations. *Mon. Wea. Rev.*, **144**, 1841–1850, <https://doi.org/10.1175/MWR-D-15-0439.1>.
- Marshall, J. H., K. Browning, J. Nicol, D. Parker, E. Norton, A. Blyth, U. Corsmeier, and F. Perry, 2010: Multi-sensor observations of a wave beneath an impacting rear-inflow jet in an elevated mesoscale convective system. *Quart. J. Roy. Meteor. Soc.*, **136**, 1788–1812, <https://doi.org/10.1002/qj.669>.
- , S. B. Trier, T. M. Weckwerth, and J. W. Wilson, 2011: Observations of elevated convection initiation leading to a surface-based squall line during 13 June IHOP\_2002. *Mon. Wea. Rev.*, **139**, 247–271, <https://doi.org/10.1175/2010MWR3422.1>.
- Mellor, G. L., and T. Yamada, 1982: Development of a turbulence closure model for geophysical fluid problems. *Rev. Geophys.*, **20**, 851–875, <https://doi.org/10.1029/RG020i004p00851>.
- Miller, R. L., 2018: Kinematics, thermodynamics, and microphysics of the 25–26 June 2015 Kansas MCS during PECAN. M.S. thesis, University of Oklahoma, Norman, OK, 154 pp.
- , C. L. Ziegler, and M. I. Biggerstaff, 2019: Seven-Doppler radar and in situ analysis of the 25–26 June 2015 Kansas MCS during PECAN. *Mon. Wea. Rev.*, **148**, 211–240, <https://doi.org/10.1175/MWR-D-19-0151.1>.
- Mlawer, E. J., S. J. Taubman, P. D. Brown, M. J. Iacono, and S. A. Clough, 1997: Radiative transfer for inhomogeneous atmospheres: RRTM, a validated correlated-k model for the longwave. *J. Geophys. Res.*, **102**, 16 663–16 682, <https://doi.org/10.1029/97JD00237>.
- Morrison, H., G. Thompson, and V. Tatarskii, 2009: Impact of cloud microphysics on the development of trailing stratiform precipitation in a simulated squall line: Comparison of one- and two-moment schemes. *Mon. Wea. Rev.*, **137**, 991–1007, <https://doi.org/10.1175/2008MWR2556.1>.
- Newton, C. W., 1950: Structure and mechanism of the prefrontal squall line. *J. Meteor.*, **7**, 210–222, [https://doi.org/10.1175/1520-0469\(1950\)007<0210:SAMOTP>2.0.CO;2](https://doi.org/10.1175/1520-0469(1950)007<0210:SAMOTP>2.0.CO;2).
- Olson, D. A., N. W. Junker, and B. Korty, 1995: Evaluation of 33 years of quantitative precipitation forecasting at the NMC. *Wea. Forecasting*, **10**, 498–511, [https://doi.org/10.1175/1520-0434\(1995\)010<0498:EOYOQP>2.0.CO;2](https://doi.org/10.1175/1520-0434(1995)010<0498:EOYOQP>2.0.CO;2).
- Parker, M. D., 2008: Response of simulated squall lines to low-level cooling. *J. Atmos. Sci.*, **65**, 1323–1341, <https://doi.org/10.1175/2007JAS2507.1>.
- , 2014: Composite VORTEX2 supercell environments from near-storm soundings. *Mon. Wea. Rev.*, **142**, 508–529, <https://doi.org/10.1175/MWR-D-13-00167.1>.
- , and R. H. Johnson, 2004a: Simulated convective lines with leading precipitation. Part I: Governing dynamics. *J. Atmos. Sci.*, **61**, 1637–1655, [https://doi.org/10.1175/1520-0469\(2004\)061<1637:SCLWLP>2.0.CO;2](https://doi.org/10.1175/1520-0469(2004)061<1637:SCLWLP>2.0.CO;2).
- , and —, 2004b: Structures and dynamics of quasi-2D mesoscale convective systems. *J. Atmos. Sci.*, **61**, 545–567, [https://doi.org/10.1175/1520-0469\(2004\)061<0545:SADOQM>2.0.CO;2](https://doi.org/10.1175/1520-0469(2004)061<0545:SADOQM>2.0.CO;2).
- Parsons, D. B., K. R. Haghi, K. T. Halbert, B. Elmer, and J. Wang, 2019: The potential role of atmospheric bores and gravity waves in the initiation and maintenance of nocturnal convection over the southern great plains. *J. Atmos. Sci.*, **76**, 43–68, <https://doi.org/10.1175/JAS-D-17-0172.1>.
- Peters, J. M., E. R. Nielsen, M. D. Parker, S. M. Hitchcock, and R. S. Schumacher, 2017: The impact of low-level moisture

- errors on model forecasts of an MCS observed during PECAN. *Mon. Wea. Rev.*, **145**, 3599–3624, <https://doi.org/10.1175/MWR-D-16-0296.1>.
- Rotunno, R., J. B. Klemp, and M. L. Weisman, 1988: A theory for strong, long-lived squall lines. *J. Atmos. Sci.*, **45**, 463–485, [https://doi.org/10.1175/1520-0469\(1988\)045<0463:ATFSSL>2.0.CO;2](https://doi.org/10.1175/1520-0469(1988)045<0463:ATFSSL>2.0.CO;2).
- Schenkman, A. D., M. Xue, and A. Shapiro, 2012: Tornadogenesis in a simulated mesovortex within a mesoscale convective system. *J. Atmos. Sci.*, **69**, 3372–3390, <https://doi.org/10.1175/JAS-D-12-038.1>.
- Schmidt, J. M., and W. R. Cotton, 1989: A High Plains squall line associated with severe surface winds. *J. Atmos. Sci.*, **46**, 281–302, [https://doi.org/10.1175/1520-0469\(1989\)046<0281:AHPSLA>2.0.CO;2](https://doi.org/10.1175/1520-0469(1989)046<0281:AHPSLA>2.0.CO;2).
- , and —, 1990: Interactions between upper and lower tropospheric gravity waves on squall line structure and maintenance. *J. Atmos. Sci.*, **47**, 1205–1222, [https://doi.org/10.1175/1520-0469\(1990\)047<1205:IBUALT>2.0.CO;2](https://doi.org/10.1175/1520-0469(1990)047<1205:IBUALT>2.0.CO;2).
- Schumacher, R. S., 2009: Mechanisms for quasi-stationary behavior in simulated heavy-rain-producing convective systems. *J. Atmos. Sci.*, **66**, 1543–1568, <https://doi.org/10.1175/2008JAS2856.1>.
- , and R. H. Johnson, 2006: Characteristics of U.S. extreme rain events during 1999–2003. *Wea. Forecasting*, **21**, 69–85, <https://doi.org/10.1175/WAF900.1>.
- , and —, 2008: Mesoscale processes contributing to extreme rainfall in a midlatitude warm-season flash flood. *Mon. Wea. Rev.*, **136**, 3964–3986, <https://doi.org/10.1175/2008MWR2471.1>.
- Skamarock, W. C., and J. B. Klemp, 2008: A time-split non-hydrostatic atmospheric model for weather research and forecasting applications. *J. Comput. Phys.*, **227**, 3465–3485, <https://doi.org/10.1016/j.jcp.2007.01.037>.
- , and Coauthors, 2008: A description of the Advanced Research WRF version 3. NCAR Tech. Note NCAR/TN-475+STR, 113 pp., <https://doi.org/10.5065/D68S4MVH>.
- Smull, B. F., and R. A. Houze, 1987: Rear inflow in squall lines with trailing stratiform precipitation. *Mon. Wea. Rev.*, **115**, 2869–2889, [https://doi.org/10.1175/1520-0493\(1987\)115<2869:RIISLW>2.0.CO;2](https://doi.org/10.1175/1520-0493(1987)115<2869:RIISLW>2.0.CO;2).
- Stull, R. B., 1988: *An Introduction to Boundary Layer Meteorology*. Kluwer Academic Publishers, 666 pp.
- Thompson, G., P. R. Field, R. M. Rasmussen, and W. D. Hall, 2008: Explicit forecasts of winter precipitation using an improved bulk microphysics scheme. Part II: Implementation of a new snow parameterization. *Mon. Wea. Rev.*, **136**, 5095–5115, <https://doi.org/10.1175/2008MWR2387.1>.
- Trapp, R. J., and M. L. Weisman, 2003: Low-level mesovortices within squall lines and bow echoes. Part II: Their genesis and implications. *Mon. Wea. Rev.*, **131**, 2804–2823, [https://doi.org/10.1175/1520-0493\(2003\)131<2804:LMWSLA>2.0.CO;2](https://doi.org/10.1175/1520-0493(2003)131<2804:LMWSLA>2.0.CO;2).
- , D. M. Wheatley, N. T. Atkins, R. W. Przybylinski, and R. Wolf, 2006: Buyer beware: Some words of caution on the use of severe wind reports in postevent assessment and research. *Wea. Forecasting*, **21**, 408–415, <https://doi.org/10.1175/WAF925.1>.
- Trier, S. B., and D. B. Parsons, 1993: Evolution of environmental conditions preceding the development of a nocturnal mesoscale convective complex. *Mon. Wea. Rev.*, **121**, 1078–1098, [https://doi.org/10.1175/1520-0493\(1993\)121<1078:EOECP>2.0.CO;2](https://doi.org/10.1175/1520-0493(1993)121<1078:EOECP>2.0.CO;2).
- Wakimoto, R. M., 2001: Convectively driven high wind events. *Severe Convective Storms, Meteor. Monogr.*, No. 50, Amer. Meteor. Soc., 255–298.
- , H. V. Murphey, C. A. Davis, and N. T. Atkins, 2006: High winds generated by bow echoes. Part II: The relationship between the mesovortices and damaging straight-line winds. *Mon. Wea. Rev.*, **134**, 2813–2829, <https://doi.org/10.1175/MWR3216.1>.
- Wallace, J. M., 1975: Diurnal variations in precipitation and thunderstorm frequency over the conterminous United States. *Mon. Wea. Rev.*, **103**, 406–419, [https://doi.org/10.1175/1520-0493\(1975\)103<0406:DVIPAT>2.0.CO;2](https://doi.org/10.1175/1520-0493(1975)103<0406:DVIPAT>2.0.CO;2).
- Weisman, M. L., C. Davis, W. Wang, K. W. Manning, and J. B. Klemp, 2008: Experiences with 0–36-h explicit convective forecasts with the WRF-ARW model. *Wea. Forecasting*, **23**, 407–437, <https://doi.org/10.1175/2007WAF2007005.1>.
- Wheatley, D. M., and R. J. Trapp, 2008: The effect of mesoscale heterogeneity on the genesis and structure of mesovortices within quasi-linear convective systems. *Mon. Wea. Rev.*, **136**, 4220–4241, <https://doi.org/10.1175/2008MWR2294.1>.
- , —, and N. T. Atkins, 2006: Radar and damage analysis of severe bow echoes observed during BAMEX. *Mon. Wea. Rev.*, **134**, 791–806, <https://doi.org/10.1175/MWR3100.1>.
- Xu, X., M. Xue, and Y. Wang, 2015: The genesis of mesovortices within a real-data simulation of a bow echo system. *J. Atmos. Sci.*, **72**, 1963–1986, <https://doi.org/10.1175/JAS-D-14-0209.1>.
- Zipser, E. J., 1977: Mesoscale and convective-scale downdrafts as distinct components of squall-line structure. *Mon. Wea. Rev.*, **105**, 1568–1589, [https://doi.org/10.1175/1520-0493\(1977\)105<1568:MACDAD>2.0.CO;2](https://doi.org/10.1175/1520-0493(1977)105<1568:MACDAD>2.0.CO;2).